Measurement and simulation of electrical properties of SiPM photon detectors

von

Florian Scheuch

Masterarbeit in Physik

vorgelegt der
Fakultät für Mathematik, Informatik und Naturwissenschaften
der Rheinisch-Westfälischen Technischen Hochschule Aachen

November 2012

Erstellt im
III. Physikalischen Institut A

Erstgutachter:
Univ.-Prof. Dr. rer.nat. Thomas Hebbeker

Zweitgutachter:
Univ.-Prof. Dr. rer.nat. Christopher Wiebusch

Abstract

An electrical model for a Silicon-Photomultiplier (SiPM) is adapted and investigated in this thesis. The model parameters (quenching resistance, diode capacitance, quenching capacitance and grid capacitance) have been determined using detailed impedance measurements for different SiPMs produced by Hamamatsu and Ketek. Using these parameters, Spice simulations have been performed and measured and simulated pulses were compared. Verifications of single pulses and complete pulse trains showed that the model is able to describe and simulate SiPMs appropriately. The adapted model can now be used for detector simulations and electronics development.

Zusammenfassung

In dieser Arbeit wird ein elektrisches Modell eines Silizium-Photomultiliers (SiPM) verwendet und untersucht. Die Parameter (Quenching-Widerstand, Dioden-Kapazität, Quenching-Kapazität und Grid-Kapazität) dieses Modells wurden mit Hilfe von detaillierten Impedanzmessungen für verschiedene SiPMs der Firmen Hamamatsu und Ketek bestimmt. Mit Hilfe dieser Werte wurden Spice Simulationen durchgeführt und gemessene mit simulierten Signalen verglichen. Untersuchungen von Einzelpixel-Pulsen und ganzen Signalspuren ergaben, dass sich der SiPM durch das verwendete Modell adäquat beschreiben und simulieren lässt. Das Modell kann nun für Detektorsimulationen und Elektronikentwicklung verwendet werden.

Contents

List of figures iii

List of tables vii

1 Introduction 1

2 Silicon Photomultipliers (SiPMs) 3

2.1 p-n-Junction 3

2.2 Geiger-Avalanche-Photodiode (G-APD) 6

2.3 Silicon-Photomultiplier (SiPM) 8

2.4 Electrical Model of SiPMs according to F. Corsi et al. 10

3 Measurements 14

3.1 Measurement device 14

3.2 Measured SiPMs 16

3.3 Raw data 17

3.3.1 Measurements under Forward Bias 17

3.3.2 Measurements under Reverse Bias 18

4 Data analysis 24

4.1 Determination of R_{Q} 24

4.2 Extraction of model parameters 26

4.3 Results for C_{D} 28

4.3.1 Depletion depth 30

4.3.2 Doping 31

4.4 Results for C_{Q} 33

4.5 Results for C_{G} 36

5 Recovery Time 38

5.1 Determination of the recovery time from electrical parameters 38

5.2 Determination of the recovery time from dark noise 38
5.2.1 Setup 40
5.2.2 Measurement and results 44

6 SiPM Simulation **48**
6.1 Electrical Simulations with Spice 48
6.2 Simulations with the SiPM model 48
6.2.1 Implementation of the initial model 48
6.3 Results 51
6.4 Test of measurement and analysis accuracy 53
6.5 Analysis of model parameters 54
6.5.1 Variation of the quenching resistance R_{Q} 55
6.5.2 Variation of the diode capacitance C_{D} 55
6.5.3 Variation of the quenching capacitance C_{Q} 56
6.5.4 Variation of the grid capacitance C_{G} 57
6.6 Correlation between grid and quenching capacitance 58
6.7 Simulations with adjusted parameters 59
6.8 Simulation of an event with crosstalk and afterpulsing 63

7 Conclusion and Outlook **65**

Bibliography **67**

A Appendix **67**
A.1 Fully derived impedance formula 67
A.2 Additional figures 67

List of Figures

1.1 Hamamatsu SiPM with $3 \cdot 3$ mm^2 size, 100 μm cell pitch [1] 1

2.1 Schematic band diagram, density of states, Fermi-Dirac distribution, and carrier concentrations for (a) intrinsic, (b) n-type, (c) p-type semiconductors at thermal equilibrium with n_i the intrinsic carrier density, N_A the acceptor impurity concentration, N_D the donator impurity concentration [2, p. 24] 4
2.2 P-n-junction in thermal equilibrium without bias voltage [3] 6
2.3 Sketch of the longitudinal structure of a G-APD [4] 7
2.4 Close up view on three types of Hamamatsu SiPMs with 100, 50 and 25 μm pixel pitch [5, modified] 9
2.5 Schematic view on direct and indirect crosstalk events [6, modified], red: incident photon, blue: secondary photons 10
2.6 Equivalent circuit of the SiPM model 12
2.7 Equivalent circuit of the SiPM model with applied forward bias voltage at low test frequency ($f < 10$ kHz) 13

3.1 Agilent 4980E LCR-Meter [7] 14
3.2 Circuit diagram of the auto-balancing bridge method [8, p. 2-3] 15
3.3 Impedance measurement with applied 2 V forward bias of the Hamamatsu SiPM No. 1549 ($1 \cdot 1$ mm^2 area, 100 μm pixel pitch) 17
3.4 Impedance measurement with applied reverse bias voltage of the Hamamatsu SiPM No. 516 ($3 \cdot 3$ mm^2 area, 100 μm pixel pitch) 19
3.5 Impedance measurement with applied reverse bias voltage of the Ketek SiPM ($3 \cdot 3$ mm^2 area, 50 μm pixel pitch) - The voltages marked with "*" are above the breakdown voltage of this device 20
3.6 Impedance measurement with applied reverse bias voltage of the Hamamatsu SiPM No. 516 ($3 \cdot 3$ mm^2 area, 100 μm pixel pitch) at 10 kHz test frequency . . . 21
3.7 Impedance measurement at 0 V reverse bias for all SiPMs 22

3.8 Impedance measurement at 20 V reverse bias for all SiPMs 23

4.1 Measured R_Q values, errors are too small to show up (Black square: Ketek SiPM, Triangles: Hamamatsu SiPMs) 25
4.2 Impedance measurement with applied fit of the impedance formula at zero bias voltage (SiPM SN: 516, $3 \cdot 3$ mm^2, 100 μm Hamamatsu) 27
4.3 Residuas of the fit of the impedance formula (SiPM SN: 516, $3 \cdot 3$ mm^2, 100 μm Hamamatsu) 27
4.4 C_D at different reverse bias voltages for all SiPMs 28
4.5 Depletion depth at different reverse bias voltages 30
4.6 $1/C_D^2$-V curve and fits for the Hamamatsu SiPM 516; the three regimes are marked, the transition regions between these regimes are clearly visible 32
4.7 Measured C_Q values, (Black square: Ketek SiPM, Triangles: Hamamatsu SiPMs) 34
4.8 Measured grid capacitances C_G, (Black square: Ketek SiPM, Triangles: Hamamatsu SiPMs) 36

5.1 Scheme of an SiPM pulse, dashed line: $\frac{1}{e}$ of the maximum signal height; green: time constant of this pulse 39
5.2 Picture of parts of the setup for recovery time determination via oscilloscope . 40
5.3 Sketch of setup for recovery time determination via oscilloscope 41
5.4 Circuit of the connection board [9, Slightly modified] 42
5.5 Amplification measurement of the Phillips scientific amplifier with a R & S FSH4 spectrum analyzer 43
5.6 A) Part of an unprocessed voltage trace; B) Part of a flattened voltage trace (the reduction of the noise-level can be seen best in the baseline); C) Part of the derivative of a voltage trace (the peaks at the beginning of the pulses are clearly visible; the negative peaks at the falling edge of the pulses are too small to be visible because the falling edge is less steep then the rising edge); for an illustration of the data processing steps at one single pixel see figure A.5 in the appendix 45
5.7 Histogram of measured recovery time constants (τ) for the Hamamatsu SiPM SN: 1549 (1x1,100) 46
5.8 All measured and derived SiPM recovery time constants τ 47

6.1 Screen capture of a typical LTSpice input; the yellow boxes represent pixels of the SiPM (cf. figure 6.2); pixels that do not fire a signal are grounded at the "V_breakdown" port; the upper left pixel is fired via the "Avalanche breakdown trigger source" 49
6.2 Screen capture of the LTSpice input for a single pixel 50
6.3 Simulation and measurement of a single photon SiPM pulse of a Hamamatsu SiPM (3x3,100), SN: 516 with the original model, simulation signal is rescaled that simulation and measurement release the same amount of charge 52
6.4 Relative deviation of the impedance measurement to the simulation for the Hamamatsu SiPM SN: 516 (3x3, 100) 53
6.5 Resulting pulse shapes for different quenching resistances for a 100 pixel SiPM (electrical parameters see table 6.3) 56
6.6 Resulting pulse shapes for different diode capacitances for a 100 pixel SiPM (electrical parameters see table 6.3) 57
6.7 Resulting pulse shapes for different quenching capacitances for a 100 pixel SiPM (electrical parameters see table 6.3) 58
6.8 Resulting pulse shapes for different grid capacitances for a 100 pixel SiPM (electrical parameters see table 6.3) 59
6.9 Pulse shape for the three different cases $\tau_Q >=< \tau_G$; in case of non-equal values the values differ approximately by a factor 4 60
6.10 Simulated and measured pulse shape for a single pixel breakdown of the Hamamatsu SiPM SN: 1067 (1x1, 25) 61
6.11 Simulated and measured pulse shape for a single pixel breakdown of the Hamamatsu SiPM SN: 1927 (1x1, 50) 62
6.12 Simulated and measured pulse shape for a several single pixel breakdowns and a crosstalk event of the Hamamatsu SiPM SN: 1067 (1x1, 25); only one pixel fires for the first four pulses 63
6.13 Simulated and measured pulse shape for a several single pixel breakdowns and a crosstalk event of the Hamamatsu SiPM SN: 1067 (1x1, 25); every pulse is triggered by a different pixel 64

A.1 Simulated and measured pulse shape for a single pixel breakdown of the Hamamatsu SiPM SN: 1549 (1x1, 100) 67

A.2 Simulated and measured pulse shape for a single pixel breakdown of the Hamamatsu SiPM SN: 516 (3x3, 100) 68
A.3 Simulated and measured pulse shape for a single pixel breakdown of the Hamamatsu SiPM SN: 551 (3x3, 100) 68
A.4 Simulated and measured pulse shape for a single pixel breakdown of the Hamamatsu SiPM SN: 1068 (1x1, 25) 69
A.5 A) Part of an unprocessed SiPM pulse within a voltage trace; B) Part of a flattened SiPM pulse within a voltage trace; C) Part of the derivative of an SiPM pulse within a voltage trace (the peak at the beginning of the puls is clearly visible; the negative peak at the falling edge of the pulse is too small to be visible because the falling edge is less steep then the rising edge) 70

List of Tables

3.1 Measurement methods and accuracy of the E4980A LCR-Meter, the measurement method “Long” provides a more accurate test signal voltage, that has no effect on the measurement accuracy [10], the “Time for a sweep” is the time for an impedance measurement with 201 data points in the frequency range from 20 Hz to 2 MHz 15

3.2 Measured SiPMs and measuring temperature 16

3.3 Impedance variation of all measured SiPMs at 2 V forward bias in the frequency range from 20 Hz - 2 MHz 18

4.1 Impedance variation of all measured SiPMs at 2 V forward bias at a frequency of 20 Hz. 24

4.2 Extrapolated diode capacitance at operating voltage (72.5 V for Hamamatsu SiPMs, 28 V for the Ketek SiPM) 29

4.3 Doping concentration in three different regimes 32

4.4 Results for the quenching capacitance for all SiPMs, the uncertainties are also gained from the fit of the impedance formula to the data (cf. section 4.2) 35

4.5 Results for the grid capacitance for all SiPMs, the uncertainties are gained from the fit of the impedance formula to the data (cf. section 4.2) 37

5.1 Resulting time constant $\tau = R \cdot C$ for all SiPMs 39

5.2 Recovery time constant determined from the dark noise signal trace (τ_{trace}) and electrical parameters (τ_{el}, cf. table 5.1) 47

6.1 Resistance values used to discharge the diode capacitance in the simulations, the values for the diode capacitance C_{D} are taken from the extraction of the electrical parameters (see section 4.3) 51

6.2 Simulation input parameters and measured values for the measurement sensitivity; The simulation marked with * is the simulation with the measured parameters 54

6.3 Simulation parameters for the analysis of the model parameter's impact on the SiPM signal 55

1 Introduction

Silicon-Photomultipliers (SiPM, see figure 1.1) have become important devices for light detection in different areas of physics.
Particle physics, for instance, uses this device for the detection of light induced by elementary particles in different collider experiments such as CMS at the LHC [11]. Here the SiPMs currently replace the previously used photomultiplier tubes (PMT) that have been established for many decades for light detection in particle physics, but show weaknesses due to their dependency on magnetic fields and the need for high bias voltages ($\sim$ 1000 V [12]).

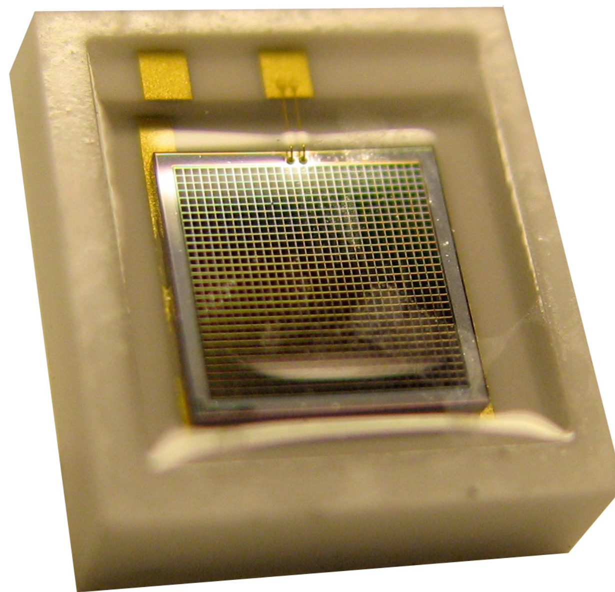

Figure 1.1: Hamamatsu SiPM with $3 \cdot 3$ mm^2 size, 100 μm cell pitch [1]

The Auger collaboration currently develops a SiPM based fluorescence light detector named FAMOUS which detects atmospheric air showers and measures the longitudinal shower shape. By this they can make conclusions about the initial cosmic particles that induced the measured air shower. Currently, these measurements are taken with a telescope that uses PMTs

to detect the light [13]. The new approach using SiPMs allows smaller setup dimensions and will increase financial efficiency in the future.
The FACT experiment is a Cherenkov telescope that uses Geiger-mode avalanche photo diodes (G-APDs) which are also used in SiPMs (see section 2) for Cherenkov light detection in air showers. A prototype has already been tested using 144 G-APDs. The final version is planned to use 1440 G-APDs [14].
Another field of application is medical physics that uses SiPMs e.g. for positron emission tomography (PET) where a good time resolution is crucial to obtain a sufficient picture resolution [15]. Since new SiPMs have a time resolution ~ 100 ps [16], they are the perfect devices for PET. The small dimensions of SiPMs allow them to be used in compact devices that are suitable for hospitals.
However, the use of SiPMs also leads to major challenges. The noise rate at room temperature is significantly higher than for PMTs. Furthermore, the measured pulses have to be corrected for after-pulsing and optical crosstalk. In addition, the SiPMs dark noise and signal is strongly temperature dependent [17].
All different applications use different types of readout electronics that decouples, amplifies and evaluates the SiPM signals. These devices have to be highly adapted to the used SiPMs. Therefore, a detailed knowledge about the SiPMs is needed, in particular the electrical properties of this photon detector. In this thesis these properties are investigated and an equivalent circuit and simulations of the electrical parameters are provided. This knowledge can help to design new readout electronics that operates SiPMs at their optimal conditions.

2 Silicon Photomultipliers (SiPMs)

2.1 p-n-Junction

A semiconductor is a material with a small (~ eV [2, p. 14]) band-gap between the conduction and the valence band. In a pure semiconductor almost all electrons are located in the valence band at low temperature. If the temperature rises, some electrons move to the conduction band and contribute to the charge carriage due to thermal excitation. The carrier concentration goes with

$$n = \int_{E_C}^{\infty} N(E)\, F(E)\, dE \tag{2.1}$$

with

$$N(E) \propto (E - E_C)^{1/2} \tag{2.2}$$

and

$$F(E) = \frac{1}{1 + \exp(\frac{E - E_F}{kT})} \tag{2.3}$$

the Fermi-Dirac distribution [2, p. 17] with n the number of charge carriers per volume, E_F the Fermi energy, $N(E)$ the total number of states, E_C the lowest energy level of the conduction band, k the Boltzman constant, T the temperature. For a schematic view of these quantities see figure 2.1

Thus the number of electrons in the conduction band increases with the temperature according to Fermi-Dirac statistics and the conductivity of the semiconductor also rises [18, p. 1].

Doping is a method to add impurities to the semiconductor. During this process the pure semiconductor (e.g. Silicon (Si)) is irradiated with an ion-beam (e.g. Phosphorus (P)) so that some of the Si-atoms in the lattice of the wafer are replaced by P-atoms [19]. Normally the dopant is a material with one valence electron more or less than the doped material. In the given example Silicon has four and Phosphorus has five valence electrons. This type of doping is called n-doping (n = negative) since the dopant introduces an additional valence electron. In this case the dopant is called donator. The other type of doping is called p-doping (p = positive) because the dopant introduces a hole in the lattice compared to the doped ma-

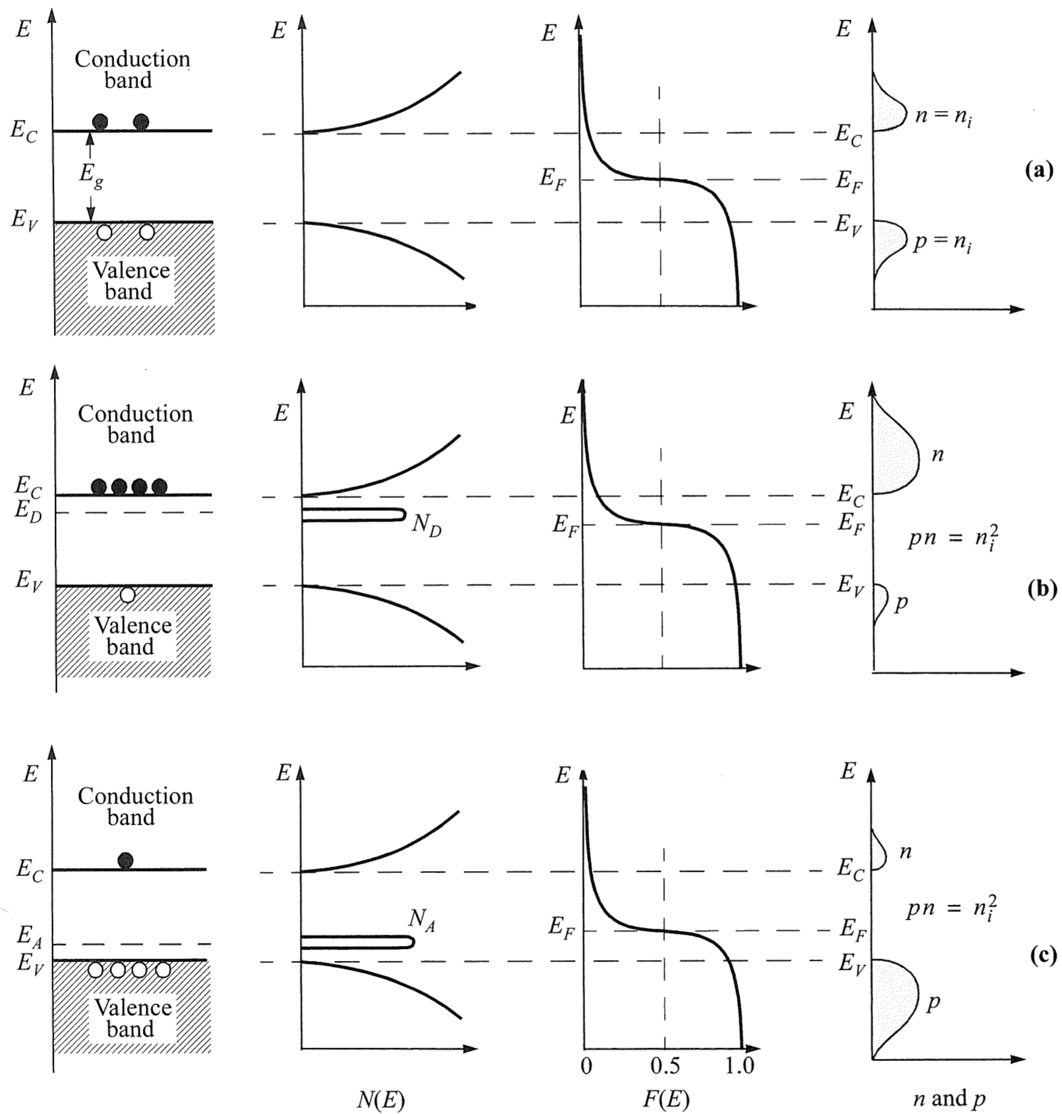

Figure 2.1: Schematic band diagram, density of states, Fermi-Dirac distribution, and carrier concentrations for (a) intrinsic, (b) n-type, (c) p-type semiconductors at thermal equilibrium with n_i the intrinsic carrier density, N_A the acceptor impurity concentration, N_D the donator impurity concentration [2, p. 24]

terial. This dopant is called acceptor.
The Fermi energy is the maximum energy of electrons at zero temperature [20]. Below this level all states are filled and no state above that level is occupied. Since the p-doped semiconductor has a lack of valence electrons, the Fermi level is lower than in the corresponding pure or n-doped semiconductor and vice versa [2, p. 27].
By attaching an n-doped and a p-doped semiconductor to each other a concentration gradient of valence electrons occurs. This gradient gets balanced by diffusion of electrons from the n- to the p-doped material (see figure 2.2). By this diffusion process the Fermi levels in both materials align. Since the Fermi level in the semiconductors is directly related to the level of the valence- and conduction-band, the level of these bands now differ between the p- and the n-doped material. This causes a gradient in the electrical potential, the so-called built-in-voltage (V_{bi}). The n-doped border region is now positively charged (anode) and vice versa (cathode). The whole intrinsically charged area is called depletion zone.
The width of the depletion zone given by

$$W_D = \sqrt{\frac{2\epsilon_{Si}\epsilon_0}{qN}\left(V_{\text{bi}} - \frac{2kT}{q}\right)} \tag{2.4}$$

where ϵ_0 is the dielectric constant, $\epsilon_{\text{Si}}(\sim 12)$ is the dielectric constant of silicon, k the Boltzmann constant, T the temperature of the junction, q the charge of a single charge carrier and N the doping concentration with $N \approx N_D$ if $N_D \ll N_A$ (N_D donator-, N_A acceptor concentration) and vice versa, is depending on the doping concentration and the built-in-voltage of the p-n-junction. This formula can be derived using the Poisson equation and assuming to have a boxed depletion profile and a single sided abrupt junction [2, p. 80 ff.].
If an external voltage is applied to this p-n-junction in such a way that the n-doped semiconductor is connected to the negative voltage and the p-doped area to the positive voltage (so-called forward bias voltage, $V_{\text{app}} > 0$), the width of the depletion zone decreases. If the external voltage exceeds the built-in-voltage, the depletion zone vanishes and the p-n-junction becomes conductive. If the voltage is applied in the opposite way (reverse bias voltage, $V_{\text{app}} < 0$) the depletion zone increases with increasing voltage. So the p-n-junction behaves as a diode.
For this case the formula for the depletion depth has an additional term

$$W_D = \sqrt{\frac{2\epsilon_{Si}\epsilon_0}{qN}\left(V_{\text{bi}} - V_{\text{app}} - \frac{2kT}{q}\right)} \tag{2.5}$$

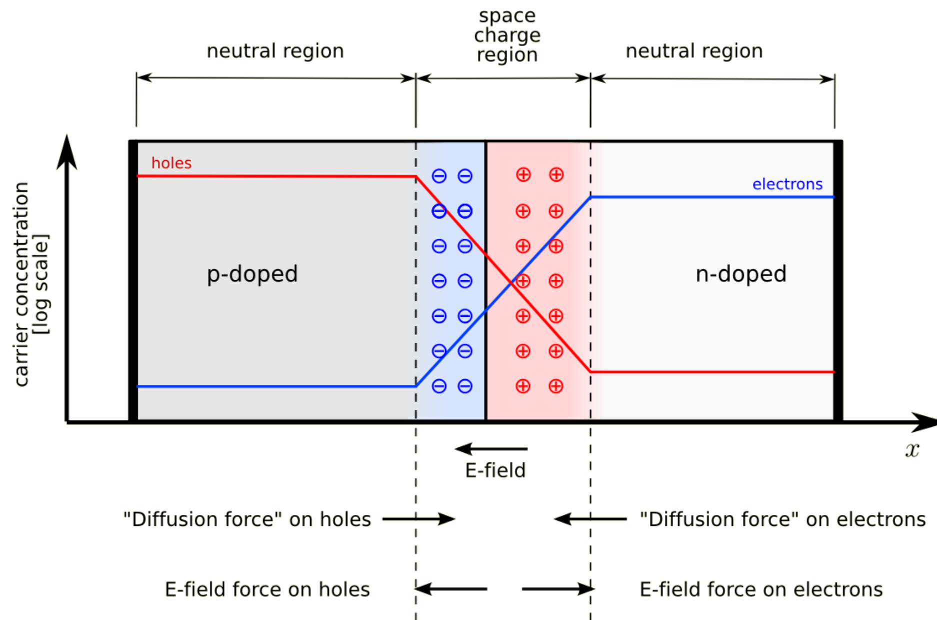

Figure 2.2: P-n-junction in thermal equilibrium without bias voltage [3]

with the external applied voltage (V_{app}) [2, p. 85].

2.2 Geiger-Avalanche-Photodiode (G-APD)

One field of application for the diode is the photodiode (PD). If a photon hits the depleted zone and creates an electron-hole-pair, the electron and the hole are accelerated in opposite directions due to the intrinsic electric field within the depleted region. These moved charges can be measured as a current between anode and cathode. These currents are in the order of magnitude of 10^{-18} A for fluxes of a few photons per second.
For small photon fluxes the current is too low for measurements. A better way to measure single photons is the Avalanche-Photodiode (APD). The APD is operated at reverse bias voltage. If the reverse bias is high enough (above the so-called breakdown-voltage) a single electron-hole-pair can trigger an avalanche of electrons and holes. The accelerated electrons and holes can excite new electron-hole-pairs by themselves due to the gain of kinetic energy that occurs because of the high electric field induced by the reverse bias voltage. A self-sustaining avalanche occurs. If the measured amount of charge is the same for different photon ener-

gies and variable numbers of incident photons, the APD is operated in the Geiger regime as a so-called Geiger-Avalanche-Photodiode (G-APD).

The avalanche must be stopped to prevent the G-APD from driving an excessive current due to the self-preserving avalanche which would destroy the device. A simple method to stop an occurring avalanche is to add an ohmic resistance in line with the G-APD. The resistance of the G-APD drops when an avalanche is triggered. The bias voltage now falls off at the ohmic resistance. The G-APD is not operated above the breakdown-voltage anymore and the avalanche stops [21].

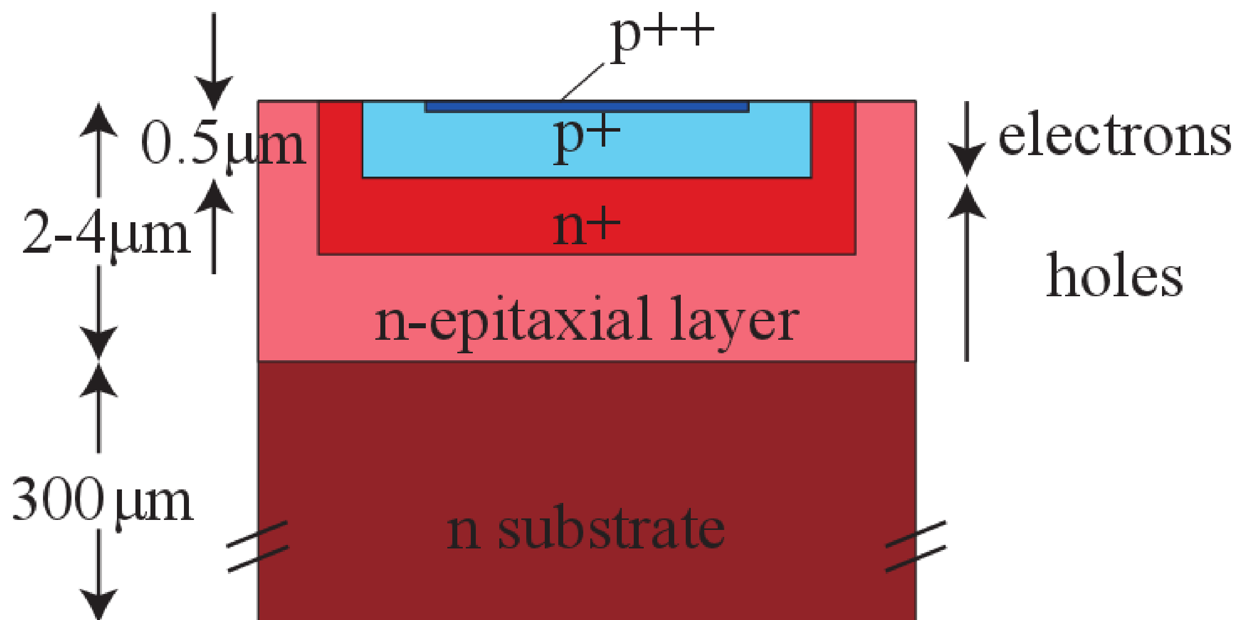

Figure 2.3: Sketch of the longitudinal structure of a G-APD [4]

Due to the production steps and the designated uniformity of the electrical field the structure of a G-APD differs slightly from a simple p-n junction as shown in figure 2.3. The structure is explained for a p-on-n structure, but is invertible depending on which wavelength the G-APD should be sensitive to (p-on-n for short wavelengths and vice versa [22]).

The G-APD is based on an n-doped substrate with $\sim 300\ \mu m$ thickness. On top of this substrate an epitaxial n-doped layer $(2-4\mu m)$ is grown with low doping concentration for production reasons with no eminent function. The highly doped p-n structure is placed on top of this layer. This structure has the function of charge multiplication as previously explained

in this section. At the surface of the G-APD an even higher doped p-region is added to achieve a good uniformity of the electrical field in the p-n layer [22].
For production reasons the quenching resistor that is often made of polysilicon or SiC is usually placed on the surface of the G-APD [23, 24]. This makes it easy to handle the resistor but limits the active area of the pixel since the resistor is not transparent and absorbs incoming photons instead of detecting them.

2.3 Silicon-Photomultiplier (SiPM)

On the one hand, the high reverse bias voltage of G-APDs results in a high photon detection efficiency (PDE) compared to common APDs. On the other hand, a single G-APD is not able to distinguish between different numbers of incident photons. To solve this problem large arrays of parallel connected G-APDs called Silicon-Photomultiplier (SiPM) are introduced.
The amplitude of the output signal is then proportional to the number of fired G-APDs and thus in a first approximation proportional to the number of incident photons as long as the number of incident photons is significantly smaller than the number of G-APDs on the SiPM.
Like photomultiplier tubes (PMTs) the SiPM can detect and process a variable amount of light and give a corresponding output signal. Furthermore, the SiPM needs a significantly smaller bias voltage (~ 30-70 V [25]) than the PMT (~ 2 kV). Other differences of SiPMs compared to PMTs are their insensitivity to magnetic fields [26] and their small dimensions. On the other hand, the SiPM's behavior is extremely temperature dependent and the noise rate at room temperature is higher than the noise rate of PMTs.
Due to the electronics (especially quenching resistors and connection wires) on top of the SiPM (see also figure 2.4) the active area is limited. The relative area of the SiPM that is still sensitive to light and not covered is called fill factor. The fill factor for common SiPMs usually varies between 30-80 % depending on the pixel size (cf. e.g. [16]).
In this thesis different terms and definitions relating to SiPM dimensions are used. The detector size is the size of the entire light sensitive area of the SiPM. The pixel pitch is the length of the edge of a single pixel on the SiPM. The definitions are also explained in figure 2.4.
Noise with respect to SiPMs are signals that are not distinguishable from those that are induced by a detected photon but have a different reason. Three phenomena contribute to this noise:
1) An electron-hole-pair can also be induced by thermal excitation within a pixel. If such a pair is excited and the avalanche is triggered, a signal is measurable at the SiPM that is indis-

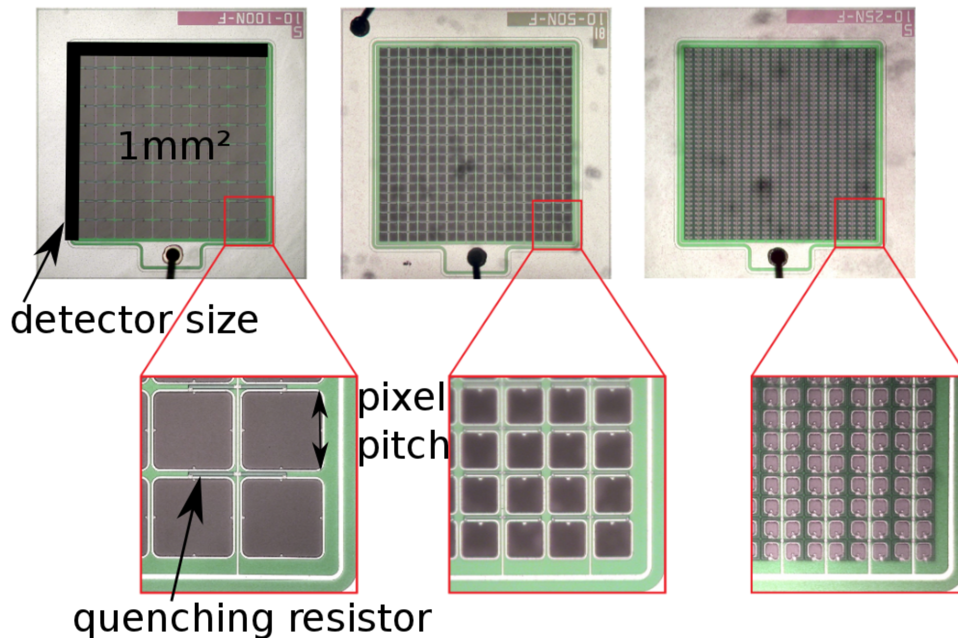

Figure 2.4: Close up view on three types of Hamamatsu SiPMs with 100, 50 and 25 μm pixel pitch [5, modified]

tinguishable from the signal induced by one photon. This is called thermal noise.
2) Another phenomenon is optical crosstalk. A pixel emits photons due to the the charge carrier multiplication during an avalanche breakdown. This light can enter other pixels and trigger an avalanche in these pixels [27]. For direct optical crosstalk the emitted photon hits another pixel directly. This type of crosstalk can be reduced e.g. by optical trenches between the pixels that absorb the photons [28]. For indirect optical crosstalk the photon is absorbed in the epitaxial layer or below and then re-emitted. This re-emitted photon hits another pixel and creates the crosstalk event. It is possible that one avalanche breakdown triggers various pixels. A schematic view of the optical crosstalk is shown in figure 2.5.
3) The third mechanism is afterpulsing. During an avalanche breakdown an electron or hole can get stuck in a metastable state on an upper energy level due to defects in the silicon lattice. If the charge carrier leaves this state after the original avalanche has been stopped, this charge carrier can induce a second avalanche breakdown in the pixel. The metastable states usually have a lifetime of $\tau \sim$ 100 ns.
The voltage that is applied to the SiPM is called bias voltage (V_{app}). The bias voltage is higher

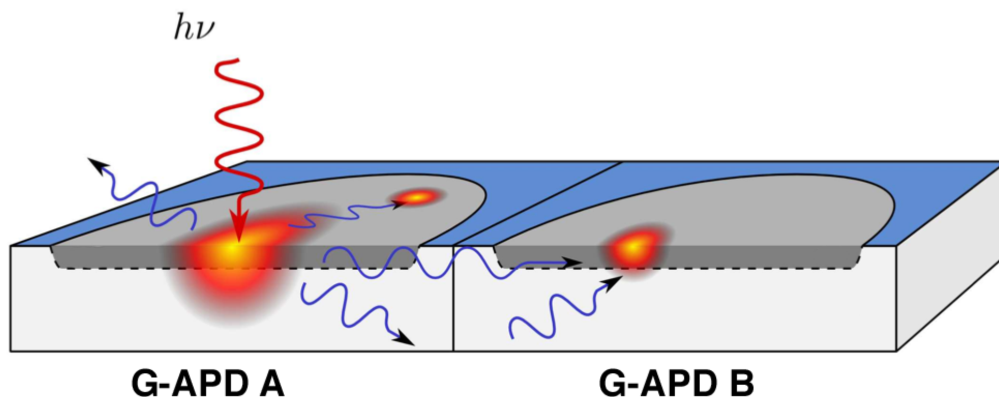

Figure 2.5: Schematic view on direct and indirect crosstalk events [6, modified], red: incident photon, blue: secondary photons

than the breakdown voltage of the device (V_{bd}) that defines the voltage when the self-preserving avalanches begin to occur. The difference of these voltages

$$V_{OV} = V_{app} - V_{bd} \tag{2.6}$$

is called over voltage (V_{OV}).

2.4 Electrical Model of SiPMs according to F. Corsi et al.

The SiPM is a complex device based on a silicon wafer. This complex configuration can be divided into different fundamental electrical devices to develop an electrical model [29].
Since the SiPM consists of many G-APDs, the model for the G-APD corresponding to [29] is discussed.
The G-APD's depletion zone can be considered as a parallel-plate capacitor with the capacitance

$$C_D = \frac{\epsilon_0 \, \epsilon_{Si} \, A}{W_d} \tag{2.7}$$

where ϵ_0 is the dielectric constant, ϵ_{Si}(∼ 12) is the dielectric constant of silicon, A is the pixel size and W_d is the depth of the depleted region [2, p. 85, eq. 24],[18, p. 63, eq. 2.4]. A high ohmic resistance in parallel to the capacitor (diode resistance, R_D) is neglected since the impedance of this resistor is expected to be much larger (∼ 100 GΩ [30]) compared to the

diode capacitance even for low frequencies and thus has no impact in a parallel circuit.
Using eq. 2.7 and 2.5 the diode capacitance can be rewritten, now depending on the applied bias voltage V_{app}

$$C_{\text{D}} = A\sqrt{\frac{Nq\epsilon_0\epsilon_{\text{Si}}}{2}}\left(V_{\text{bi}} - V_{\text{app}} - \frac{2kT}{q}\right)^{-\frac{1}{2}}. \tag{2.8}$$

Squaring and inverting yields

$$\frac{1}{C_{\text{D}}^2} = \frac{2}{q\epsilon_0\epsilon_{\text{Si}}NA^2}\left(V_{\text{bi}} - V_{\text{app}} - \frac{2kT}{q}\right) \tag{2.9}$$

that leads to the first derivative

$$\frac{d(1/C_{\text{D}}^2)}{dV_{\text{app}}} = -\frac{2}{q\epsilon_0\epsilon_{\text{Si}}NA^2} \tag{2.10}$$

that can be used to determine the doping concentration N of the lower doped side of the p-n junction. For the discussed devices it is the n-side of the junction.
Every depleted region and thus every diode capacitor has a quenching resistor in line to limit the breakdown (cf. section 2.2). This resistor is called R_{Q} in the model. The quenching resistor is not ideal and has a parasitic capacitance (C_{Q}) in parallel as every real ohmic resistor. Hence the G-APD has a quenching resistor and a quenching capacitance in parallel and a diode capacitance in line to this.
An SiPM consists of many G-APDs in parallel. So for the electrical model, n G-APDs are connected in parallel (with n the number of pixels).
The SiPM has macroscopic connection pins and connections on the wafer. These connections and wafer effects are summarized in a so-called "grid capacitance" (C_{G}) that is placed in parallel to the pixels. The resulting electrical model of the SiPM is shown in figure 2.6.
The total impedance between the connections A and B (cf. figure 2.6) for this model can be simply calculated by using Kirchhoff's circuit laws [31] and calculating the absolute value of this impedance. Deriving this function leads to

$$|Z| = \left| n\left(\left(R_{\text{Q}}^{-1} + i\omega\, C_{\text{Q}}\right)^{-1} - \frac{i}{\omega\, C_{\text{D}}}\right)^{-1} + i\omega\, C_{\text{G}}\right|^{-1} \tag{2.11}$$

with the quenching resistance R_{Q}, the quenching capacitance C_{Q}, the diode capacitance C_{D}, the grid capacitance C_{G} and the number of pixels n. The fully derived absolute value is shown

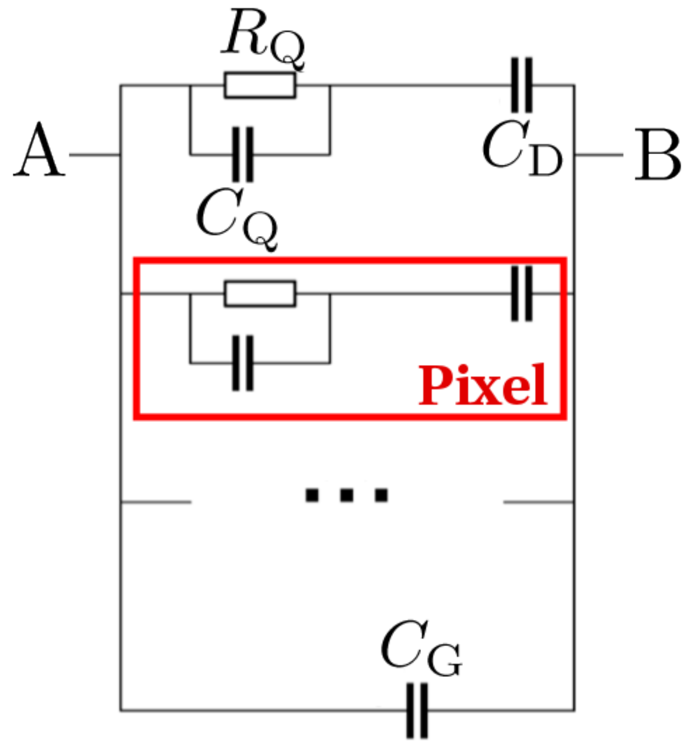

Figure 2.6: Equivalent circuit of the SiPM model

in the appendix in equation A.1. By measuring the impedance for various test frequencies and bias voltages the introduced electrical parameters can be obtained.
If the SiPM is attached to a forward bias voltage with low frequency, the model changes (see figure 2.7). The diode capacitance vanishes due to the resolving of the depletion zone. Only a small diode resistance remains that can be neglected compared to the quenching resistance. The quenching capacitance (C_Q) has a very high impedance at low frequencies. For a quenching capacitance of 10^{-13} F at 20 Hz the impedance is

$$Z_Q = \left| \frac{1}{i\omega C} \right| \approx 7.96 \cdot 10^{10} \Omega \tag{2.12}$$

which is much larger than the expected quenching resistance ($\sim$ 100 kΩ [30, p. 11]). So due to

$$Z_{sum} = \left(\frac{1}{Z_R} + \frac{1}{Z_C} \right)^{-1} \approx Z_R \tag{2.13}$$

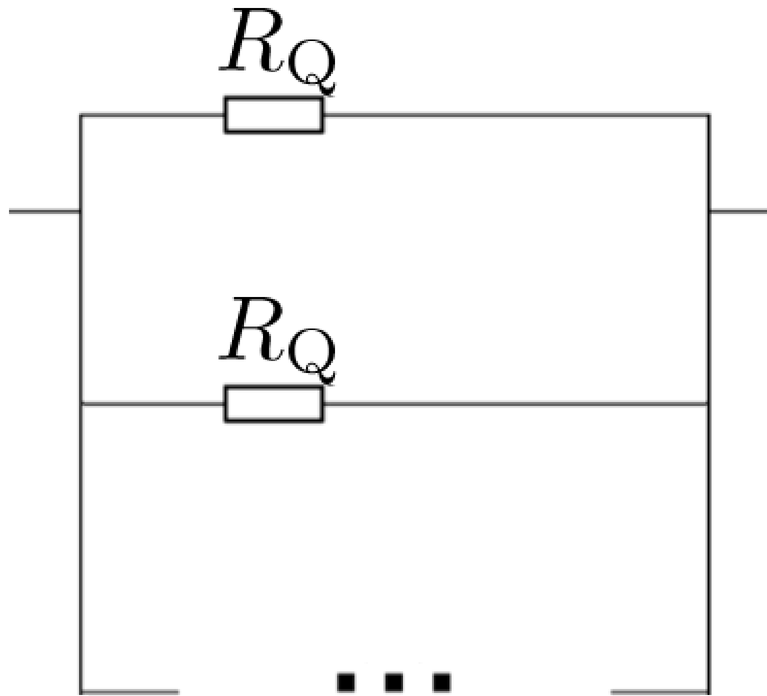

Figure 2.7: Equivalent circuit of the SiPM model with applied forward bias voltage at low test frequency (f < 10 kHz)

for $Z_R \ll Z_C$ the quenching capacitance can be neglected for low frequencies.
For the same reason the grid capacitance can be likewise neglected. Thus the electrical model for an SiPM at forward bias with low frequency is reduced to n parallel quenching resistors. By measuring the total impedance under these conditions the quenching capacitance can be determined with

$$R_Q = |Z_{total}| \cdot n. \tag{2.14}$$

3 Measurements

3.1 Measurement device

All impedance measurements were taken with the Agilent 4980E LCR meter (see figure 3.1) with a high voltage option for 40 V DC. The LCR meter outputs a sine signal and analyses the input signal to obtain the phase angle and the attenuation between output and input. These values can be displayed directly or as capacitance/inductance and resistance values presuming a serial or parallel circuit.

Figure 3.1: Agilent 4980E LCR-Meter [7]

The test frequency of this device can be varied automatically from 20 Hz up to 2 MHz in up to 201 steps, the data is stored as .xls file on an USB memory device.
Three types of measurement durations (Long, Middle, Short) are available. For purposes of this thesis only the measurement method "Middle" was used because it was a reliable compromise between accuracy and duration. The duration and accuracy for an impedance measurement from 20 Hz up to 2 MHz in 201 steps is shown in table 3.1.
To obtain a good accuracy this device takes the data using the auto-balancing bridge method (see figure 3.2). This method uses an I-V converter to measure the current through the resistor

Measurement method	Overall measurement accuracy / %	Time for sweep / s
Short	0.63	36
Middle	0.28	61
Long	0.28	109

Table 3.1: Measurement methods and accuracy of the E4980A LCR-Meter, the measurement method “Long” provides a more accurate test signal voltage, that has no effect on the measurement accuracy [10], the “Time for a sweep” is the time for an impedance measurement with 201 data points in the frequency range from 20 Hz to 2 MHz

R_r that balances with the current through the device under test (DUT). Thus the impedance can be calculated by measuring the voltage V_x and V_r. LCR-Meters with a measurement range at low frequencies use a simple operational amplifier as I-V converter. Due to their limited bandwidth a more sophisticated I-V converter has to be used for LCR meters with high measurement frequencies [8].

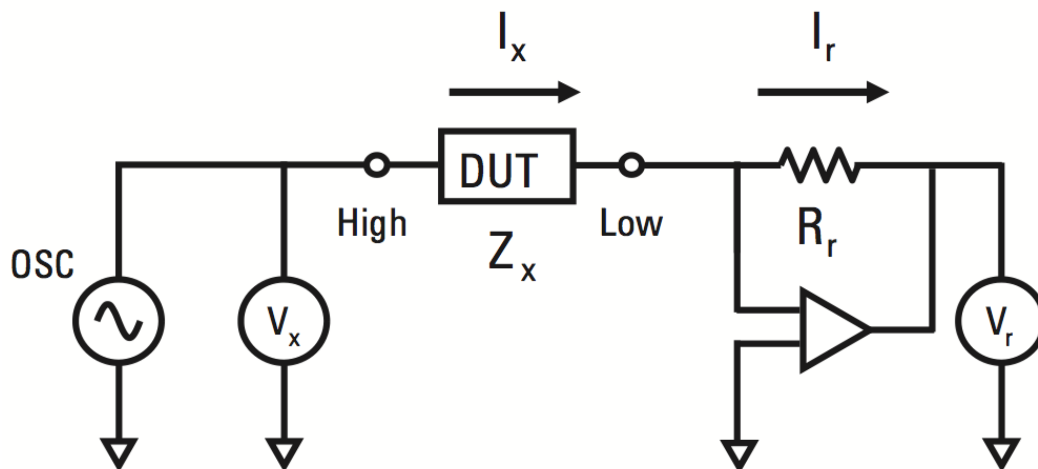

Figure 3.2: Circuit diagram of the auto-balancing bridge method [8, p. 2-3]

All measurements were taken with an input signal amplitude of (50.00±0.13) mV and have an accuracy of 0.28 % on the impedance values. This uncertainty results from the linear sum of the relative uncertainty on the measurement (0.25 %) and the calibration uncertainty (0.03 %)

Manufacturer	SiPM size / mm^2	Pixel side length / μm	Serial No.	Temperature / °C
Hamamatsu	$1x1$	100	1549	21.8
Hamamatsu	$3x3$	100	516	21.8
Hamamatsu	$3x3$	100	551	21.9
Hamamatsu	$1x1$	50	1927	22.0
Hamamatsu	$3x3$	50	2889	22.0
Hamamatsu	$1x1$	25	1067	22.0
Hamamatsu	$1x1$	25	1068	22.2
Hamamatsu	$3x3$	25	150	22.2
Ketek	$3x3$	50	N/A	21.8

Table 3.2: Measured SiPMs and measuring temperature

that remains, if the device is open- and short-corrected [10].
For the open-correction no device is attached to the LCR meter so that the capacitance of the connections can be corrected. During the short-correction the two connectors are short-circuited so that the resistance and the inductance of the connectors can be corrected.

3.2 Measured SiPMs

The different types of measured SiPMs are shown in table 3.2. Since the operating temperature is crucial for the SiPM's behavior, all measurements were carried out in a room with controlled temperature. Therefore, the temperature only varied from 21.8 °C $-$ 22.2 °C between the measurements. The temperatures at each measurement are also displayed in table 3.2.
For every SiPM the impedance was measured with a forward bias voltage of 2 V in the frequency range from 20 Hz - 2 MHz to determine the quenching resistance (see section 4.1).
To determine the other electrical parameters the impedance was measured with applied reverse bias voltage. The voltage was increased by 2 V for every measurement beginning with 0 V. The maximum measured voltage was 34 V - 40 V for the SiPMs. This is due to the fact that some measurements at voltages between 34 V and 40 V were not saved correctly on the USB data storage by the LCR meter. For the Hamamatsu SiPM with serial number 1549 and the Ketek SiPM data was taken at 1 V steps, also beginning at 0 V.
The dimensions will be displayed as <Detector Size>, <Pixel side length> in the following (e.g. 1x1, 100 for an SiPM with $1 \cdot 1$ mm^2 detector size and 100 μm pixel side length).

3.3 Raw data

In this section the raw data is discussed. For the analysis of the data and values of the electrical properties see section 4.

3.3.1 Measurements under Forward Bias

A measurement of the impedance in the range between 20 Hz and 2 MHz of the Hamamatsu SiPM No. 1549 is shown in figure 3.3.

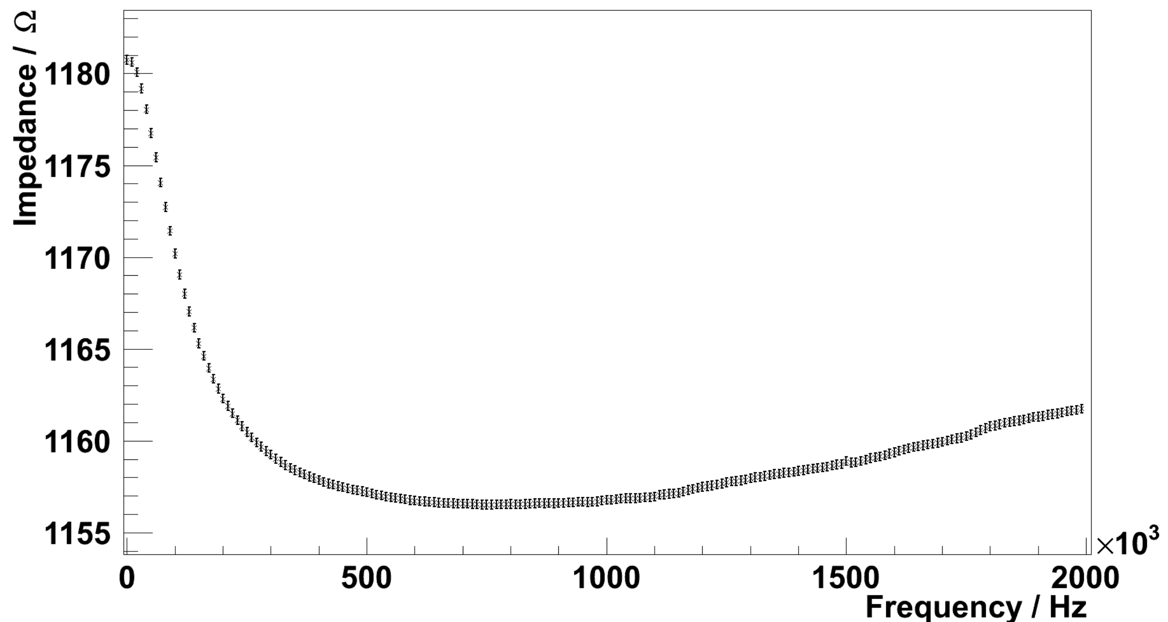

Figure 3.3: Impedance measurement with applied 2 V forward bias of the Hamamatsu SiPM No. 1549 ($1 \cdot 1$ mm^2 area, 100 μm pixel pitch)

The impedance varies about 3% over the whole frequency range. The decreasing impedance from 20 Hz to about 750 kHz indicates an unconsidered capacitance in the SiPM's equivalent circuit. The increase of the impedance from about 750 kHz to 2 MHz could be due to an inductance in line to the hitherto existing equivalent circuit. Since the variation of the total impedance is relatively small for all SiPMs, the circuit model is not adjusted, particularly because the analysis of the raw data with the explained model works fine (see section 4). The

SN.	SiPM type	Min. impedance / Ω	Max. impedance / Ω	Relative difference
1549	1x1, 100	$1.156 \cdot 10^3$	$1.181 \cdot 10^3$	2.1 %
516	3x3, 100	$1.324 \cdot 10^2$	$1.366 \cdot 10^2$	3.1 %
551	3x3, 100	$1.288 \cdot 10^2$	$1.330 \cdot 10^2$	3.2 %
1927	1x1, 50	$3.144 \cdot 10^2$	$3.217 \cdot 10^2$	2.3 %
2889	3x3, 50	$4.059 \cdot 10^1$	$4.201 \cdot 10^1$	3.4 %
1067	1x1, 25	$1.670 \cdot 10^2$	$1.722 \cdot 10^2$	3.0 %
1068	1x1, 25	$1.664 \cdot 10^2$	$1.718 \cdot 10^2$	3.1 %
150	3x3, 25	$2.263 \cdot 10^1$	$2.341 \cdot 10^1$	3.3 %
Ketek	3x3, 50	$1.015 \cdot 10^2$	$1.042 \cdot 10^2$	2.6 %

Table 3.3: Impedance variation of all measured SiPMs at 2 V forward bias in the frequency range from 20 Hz - 2 MHz

impedance variation in the forward bias measurement for all SiPMs is shown in table 3.3.
The data points at very low frequencies show that the impedance converges towards a constant value for very low frequencies corresponding to the explanation in section 2.4. Thus the impedance value at the lowest available frequency (20 Hz) is used for the determination of the quenching resistor (R_Q) as it is explained in section 4.1.

3.3.2 Measurements under Reverse Bias

A typical impedance measurement of a Hamamatsu SiPM is shown in figure 3.4. A variation of the impedance values with changing bias voltage is apparent. The impedance values vary from 20 Hz to 2 MHz by two orders of magnitude. The decreasing impedance with increasing frequency is expected because of the capacitances in the SiPM's equivalent circuit and their impedance behavior ($Z_C = \frac{1}{i\omega C}$). The variation of the impedance by the applied bias voltage is driven by the diode capacitance and its dependence on the width of the depletion zone. Corresponding to formula 2.7 the capacitance decreases with increasing reverse bias voltage because the depletion depth and accordingly the distance of the capacitor plates in the parallel plate capacitor approximation is increased. Thus the increase of the impedance for higher bias voltages is expected as well.
The variation of impedance values at bias voltages larger than 22 V is small compared to the variation below this voltage. This implies only a small decrease of the diode capacitance at voltages higher than 22 V. This might be caused by the full depletion of the pixels so that the

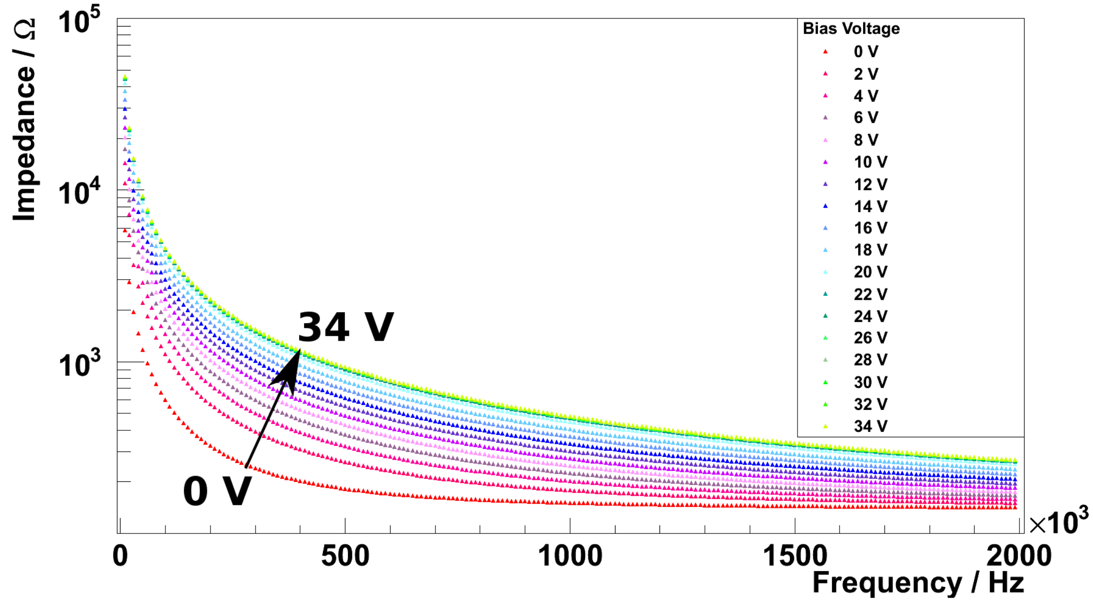

Figure 3.4: Impedance measurement with applied reverse bias voltage of the Hamamatsu SiPM No. 516 ($3 \cdot 3$ mm^2 area, 100 μm pixel pitch)

depletion zone does not increase any further above 22 V. This voltage is ~ 50 V lower than the breakdown voltage (V_{bd}) of the Hamamatsu SiPMs. This high breakdown voltage leads to a higher efficiency in detecting photons [17].

The measurement of the Ketek SiPM shows a similar behavior (see figure 3.5). But for this SiPM a full depletion is never reached and due to its low breakdown voltage at 27.9 V the impedance values above this reverse bias voltage do not correspond to the behavior of the whole equivalent circuit anymore. At high voltages the impedance values are almost constant over the whole frequency spectrum. The measurements were all conducted at full daylight due to the measurement environment that does not allow to darken the SiPM so that the SiPM is hit by photons continuously. Thus above the breakdown voltage diode breakdowns are constantly triggered and the pixels are not able to recharge. This results in a constant current through the SiPM that causes the constant impedance values.

However the impedance above the breakdown voltage slightly decreases for higher test frequencies. This is because the sum of the impedance of the quenching resistor and its parallel

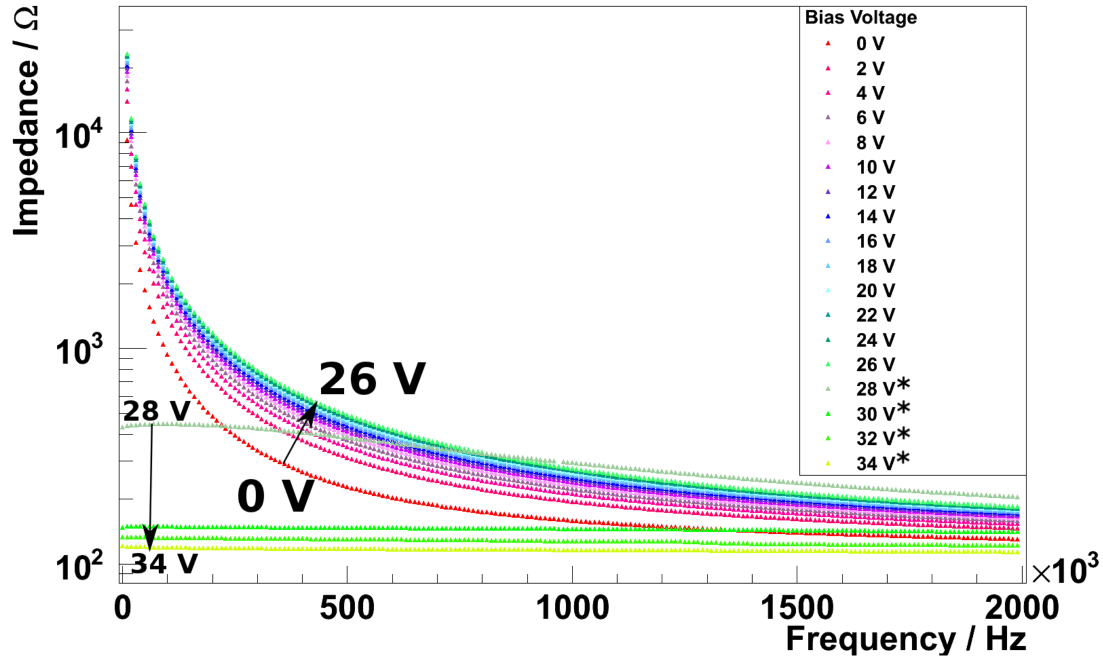

Figure 3.5: Impedance measurement with applied reverse bias voltage of the Ketek SiPM ($3 \cdot 3$ mm^2 area, 50 μm pixel pitch) - The voltages marked with "*" are above the breakdown voltage of this device

quenching capacitance

$$Z_Q = \left(\frac{1}{R_Q} + i\omega C_Q \right)^{-1} \tag{3.1}$$

decreases for higher frequencies ($f = \frac{\omega}{2\pi}$).

It is also interesting to take note of the impedance-voltage characteristic for a fixed test frequency (figure 3.6). The data points show three different regions. In the region from 0 V to 10 V the impedance increases with a lower slope than in the region from 10 V to 20 V. This difference is caused by the structure of the SiPM. At low bias voltages only the p-n junction is depleted. If the voltage is rising, the epitaxial layer (see section 2.2) is also depleted. Since the doping concentration of this layer is lower than the doping concentration of the p-n junction, more material is depleted per bias voltage step. Thus the diode capacitance decreases and the total impedance rises faster. At a reverse bias above 20 V the already discussed saturation occurs.

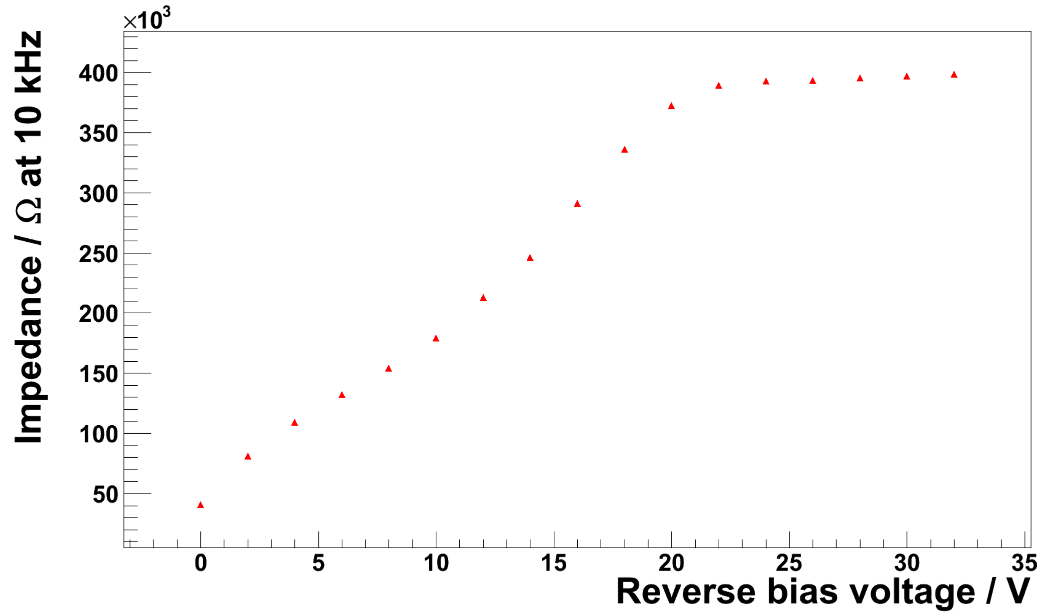

Figure 3.6: Impedance measurement with applied reverse bias voltage of the Hamamatsu SiPM No. 516 ($3 \cdot 3$ mm^2 area, 100 μm pixel pitch) at 10 kHz test frequency

It is also possible to gain information from the comparison of the impedance values for the different SiPMs at a given bias voltage (see figure 3.7).
At low frequencies the Hamamatsu SiPMs with 1 mm^2 show the same order of magnitude of impedance values. Similarly all Hamamatsu devices with 9 mm^2 size also show a similar behavior at low frequencies. If the frequency is increased, the impedance for the SiPMs with different pixel size differs. SiPMs with a large pixel size have a relatively high impedance compared to the lower pixel sizes. A low pixel size corresponds to a large number of pixels and therefore to a low impedance since

$$Z \propto \frac{1}{\mathrm{n}} \tag{3.2}$$

with the number of pixels n. Because of

$$Z_\mathrm{D} \propto \frac{1}{\omega C_\mathrm{D}} \propto \frac{1}{A} \tag{3.3}$$

with the area A of the pixel (see also section 2.4), the impedance for large pixels and therefore

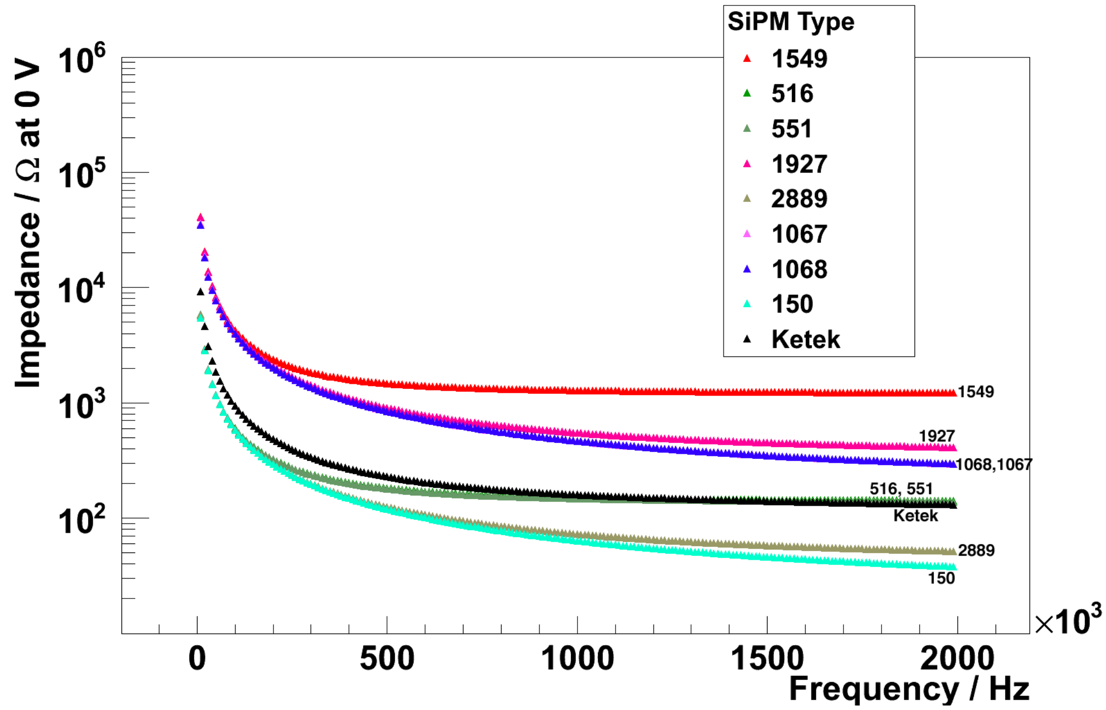

Figure 3.7: Impedance measurement at 0 V reverse bias for all SiPMs

relatively large diode capacitances saturates at high frequencies.
The Ketek SiPM shows different impedance values, but yields the same structure of the impedance frequency dependency. The higher impedance compared to the Hamamatsu SiPM with 9 mm^2 detector area and 50 μm pixel size (SN: 2889) points to a higher quenching resistance.
At a higher reverse bias voltage the impedance values for the 1 mm^2 and the 9 mm^2 Hamamatsu SiPMs each become even more similar (see figure 3.8). The diode capacitance decreases for higher reverse bias voltages. So the product ωC_{D} at e.g. 20 V reverse bias is smaller at a certain frequency compared to the product at no bias voltage. Thus the diode's impedance is larger at higher reverse bias voltages (see also equation 3.3) and therefore more dominant in the sum of the diode's and the quenching resistance's impedance. So the splitting of the impedance values between SiPMs of the same detector size but with different pixel sizes starts at higher frequencies for a high reverse bias voltage.
The impedance values of the Ketek SiPM are below the values for the 9 mm^2 Hamamatsu

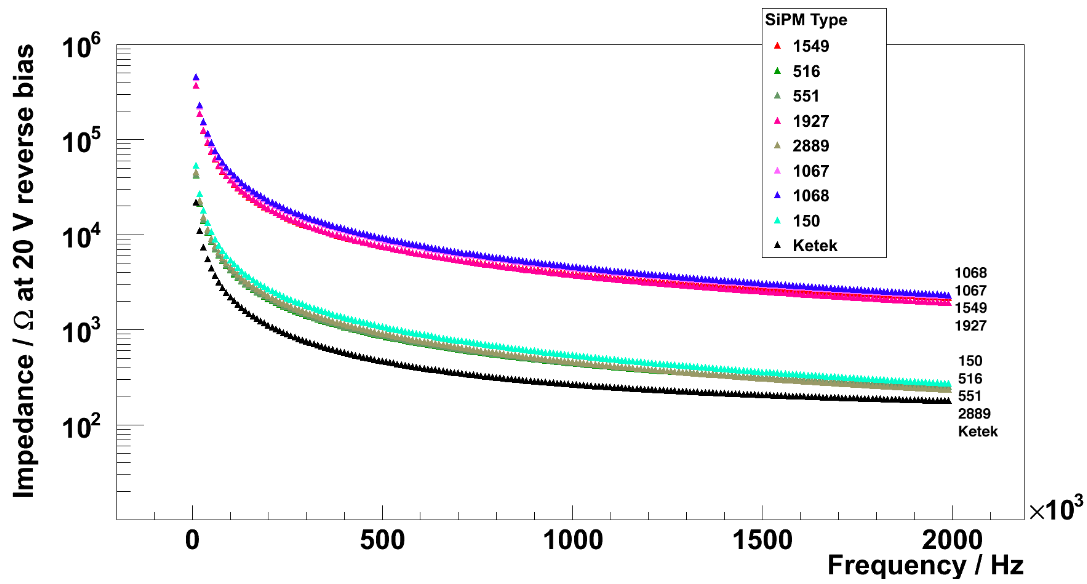

Figure 3.8: Impedance measurement at 20 V reverse bias for all SiPMs

SiPMs for 20 V reverse bias voltage. Since the values are higher than the values of the Hamamatsu SiPMs for no reverse bias voltage, this behavior points to a different diode doping in Ketek and Hamamatsu SiPMs. Otherwise one would expect the same relative position of the values for low reverse bias voltages.

4 Data analysis

4.1 Determination of R_Q

For the determination of the quenching resistance (R_Q) only the value of the measurement with applied forward bias voltage of 2 V at 20 Hz is used. This value is multiplied by the number of pixels (see equation 2.14). The uncertainty on the gained value is the error on the measurement of the total impedance multiplied by the number of pixels. A systematic uncertainty caused by other components due to the non-zero frequency ($\omega \neq 0$, cf. formula 2.11) is neglected because the impedance values move to a constant value for decreasing frequencies as explained in section 3.3.1.
The values for the quenching resistance are fixed for the next steps of the analysis. The results are shown in table 4.1 and figure 4.1.

SN.	SiPM size	Total Impedance / Ω	No. of pixels	R_Q / kΩ
1549	1x1, 100	$(1.181 \pm 0.003) \cdot 10^3$	100	118.1 ± 0.3
516	3x3, 100	$(1.366 \pm 0.004) \cdot 10^2$	900	122.9 ± 0.3
551	3x3, 100	$(1.330 \pm 0.004) \cdot 10^2$	900	119.7 ± 0.3
1927	1x1, 50	$(3.217 \pm 0.009) \cdot 10^2$	400	128.7 ± 0.4
2889	3x3, 50	$(4.201 \pm .0011) \cdot 10^1$	3600	151.2 ± 0.4
1067	1x1, 25	$(1.722 \pm 0.005) \cdot 10^2$	1600	275.5 ± 0.8
1068	1x1, 25	$(1.718 \pm 0.005) \cdot 10^2$	1600	274.9 ± 0.8
150	3x3, 25	$(2.341 \pm 0.007) \cdot 10^1$	14400	337.1 ± 0.9
Ketek	3x3, 50	$(1.042 \pm 0.003) \cdot 10^2$	3600	375.1 ± 1.1

Table 4.1: Impedance variation of all measured SiPMs at 2 V forward bias at a frequency of 20 Hz.

All measured quenching resistances are in the range from 100 kΩ to 400 kΩ and thus in the same order of magnitude that was measured by other groups [30, 9, 29], though they measured different SiPM types.
The Ketek SiPM shows a quenching resistance that is about 2.5 times higher than for the corresponding Hamamatsu SiPM. This may have an impact on the recovery time of the pixel

that is higher for the Hamamatsu SiPM as well (see section 5.1 for the analysis of the recovery time).
In general the quenching resistance seems to increase with decreasing pixel size and increasing detector size. The difference between SiPMs of the same pixel size but different detector size is larger for SiPMs with small pixels.

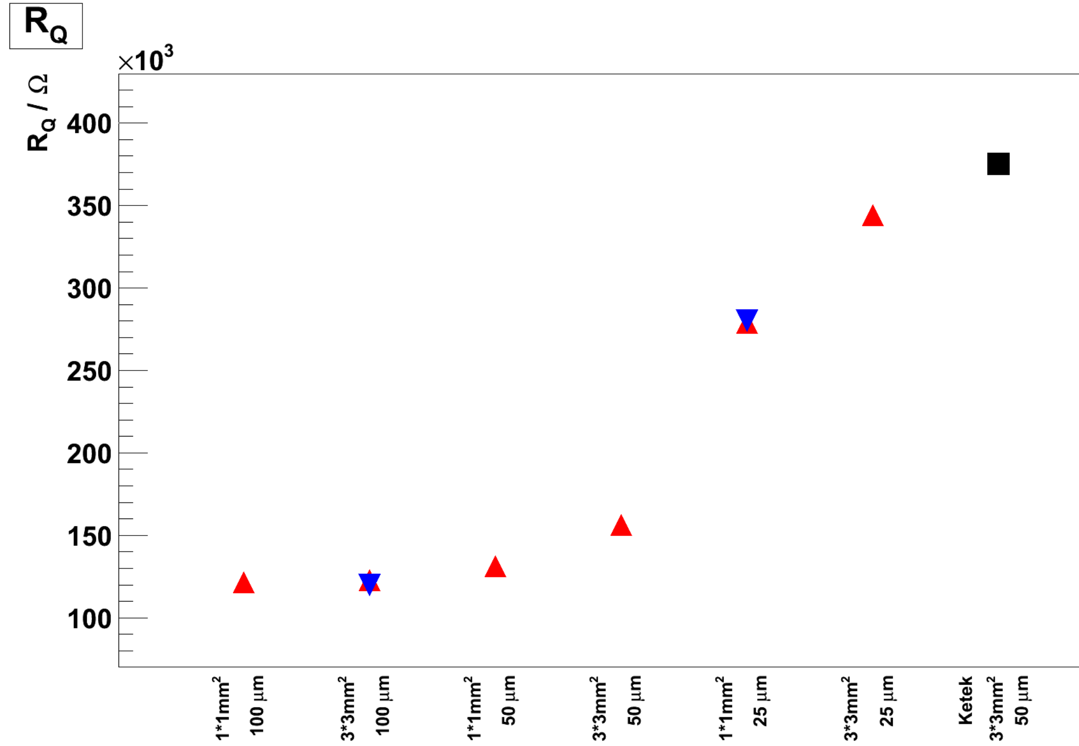

Figure 4.1: Measured R_Q values, errors are too small to show up (Black square: Ketek SiPM, Triangles: Hamamatsu SiPMs)

At low pixel sizes the geometrical size of the quenching resistor has to be reduced so that the fill factor of the SiPM does not get too low. A reduced size of the resistor's cross-sectional area automatically leads to a higher resistivity due to

$$R = \rho \frac{l}{A} \tag{4.1}$$

with the resistance R, the resistivity ρ, depth l and the cross-sectional area A [31, p. 47]. Therefore, the quenching resistance has to be increased to have a remaining sensitive detec-

tor area with small pixel sizes.
For large numbers of pixels the total resistivity of the SiPM drops because $Z_{\text{total}} \propto n^{-1}$. If an SiPM is fully illuminated, the current through the device is only limited by the quenching resistances. An SiPM with a higher pixel number has a lower total impedance compared to an SiPM with a lower pixel number but the same quenching resistance value due to the parallel setup of the pixels. So the quenching resistance has to be increased for high numbers of pixels to prevent the SiPM from driving an excessive current at full light.
This argument can also explain the increase of the difference in the quenching resistances between the 1 mm^2 and the 9 mm^2 SiPM with decreasing pixel size. For large pixel sizes the absolute number of pixels on an SiPM is low enough to even handle a factor 9 greater SiPM size without or with small quenching resistance adaption.

4.2 Extraction of model parameters

The other model parameters (C_{D}, C_{Q}, C_{G}) are determined by fits to the data. In a first step the formula for the impedance depending on the test frequency calculated from the SiPM's electrical model (see equation 2.11) is fitted to the measured data points at 0 V bias voltage. The value for the quenching resistor is fixed to the measured values for this fit (see section 4.1). This fit yields the three missing parameters. The parameters C_{Q} and C_{G} (for results see sections 4.7 and 4.8) are also fixed after this fit since it is expected that these parameters are not frequency dependent and do not depend on the applied bias voltage.
In a second step the fit is then repeated for the measurements with applied reverse bias voltage with the one free parameter C_{D}. So the diode capacitance can be determined frequency dependently.
A typical fit is shown in figure 4.2.
The residua are shown in figure 4.3. The fit shows good agreement between measurement and electrical model. At low frequencies the impedance deviates from the expected values. However, this deviation is relatively small compared to the absolute value. For 20 Hz the deviation is $\sim -0.4\%$. For higher frequencies the relative deviation increases slightly and reaches $\sim 2\%$ at 2 MHz in the shown example. This effect can be due to unknown parasitic inductances and capacitances that are not considered in the electrical model and are more relevant at very low and high frequencies, respectively, due to

$$|Z_{\text{L}}| = \omega \text{L} \tag{4.2}$$

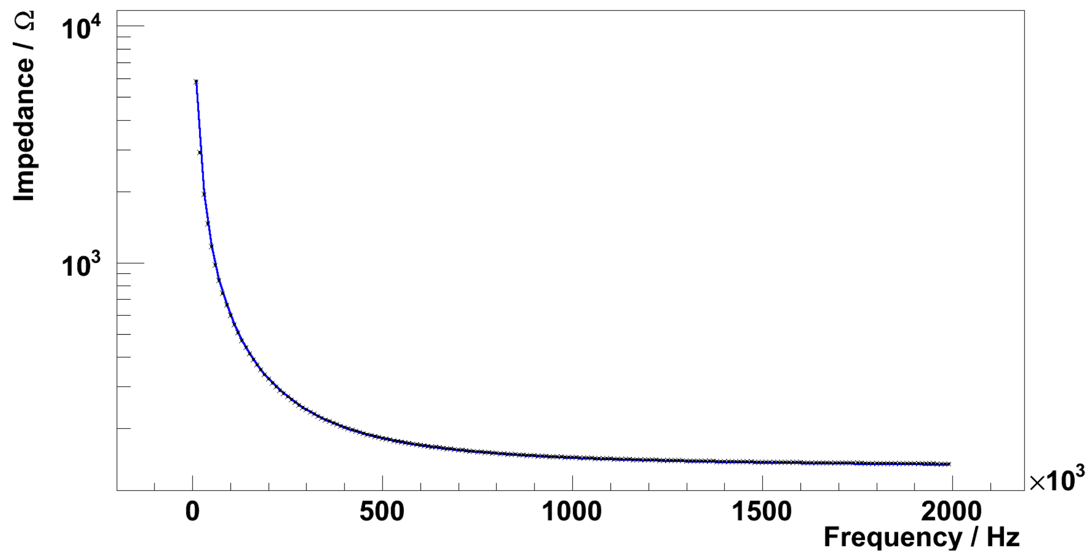

Figure 4.2: Impedance measurement with applied fit of the impedance formula at zero bias voltage (SiPM SN: 516, 3·3 mm^2, 100 μm Hamamatsu)

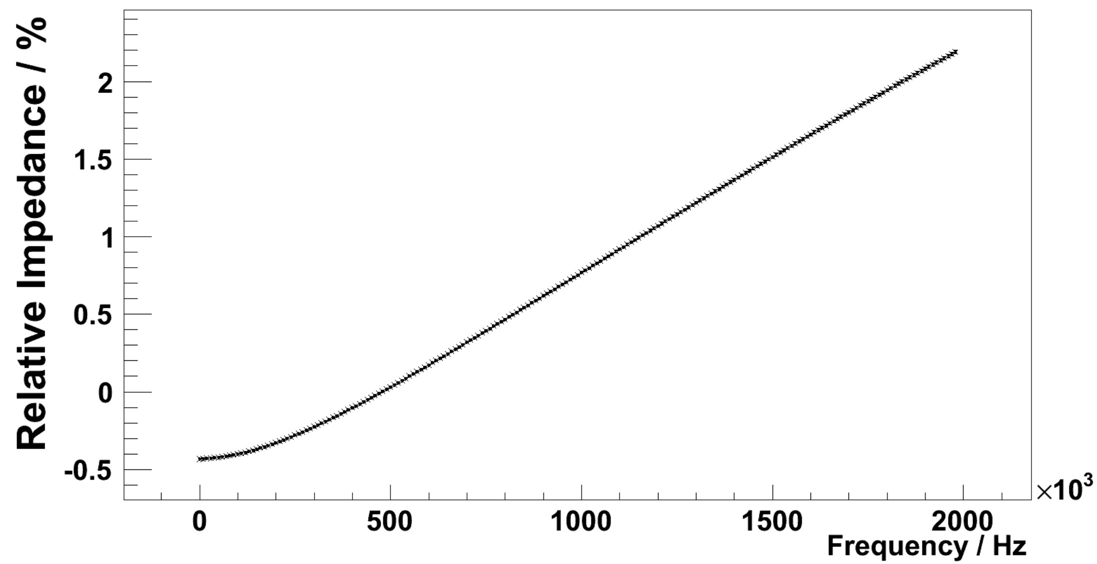

Figure 4.3: Residuas of the fit of the impedance formula (SiPM SN: 516, 3·3 mm^2, 100 μm Hamamatsu)

with the inductance L and

$$|Z_C| = \frac{1}{\omega C} \tag{4.3}$$

with the capacitance C.

4.3 Results for C_D

The diode capacitance is now measured at different reverse bias voltages. The measurement results are shown in figure 4.4. The capacitance drops with higher reverse bias voltage as it is expected since the depletion zone and thus the size of the assumed parallel plate capacitor expands with higher applied voltages. For voltages above 20 V the diode capacitance is almost constant. This indicates a full depletion of the SiPM which means that the whole G-APD including the epitaxial layer is depleted except for the substrate. This can be derived because the substrate is doped relatively highly and thus the depletion depth of this layer increases much slower for increasing applied reverse bias voltage compared to a layer with a lower doping density.

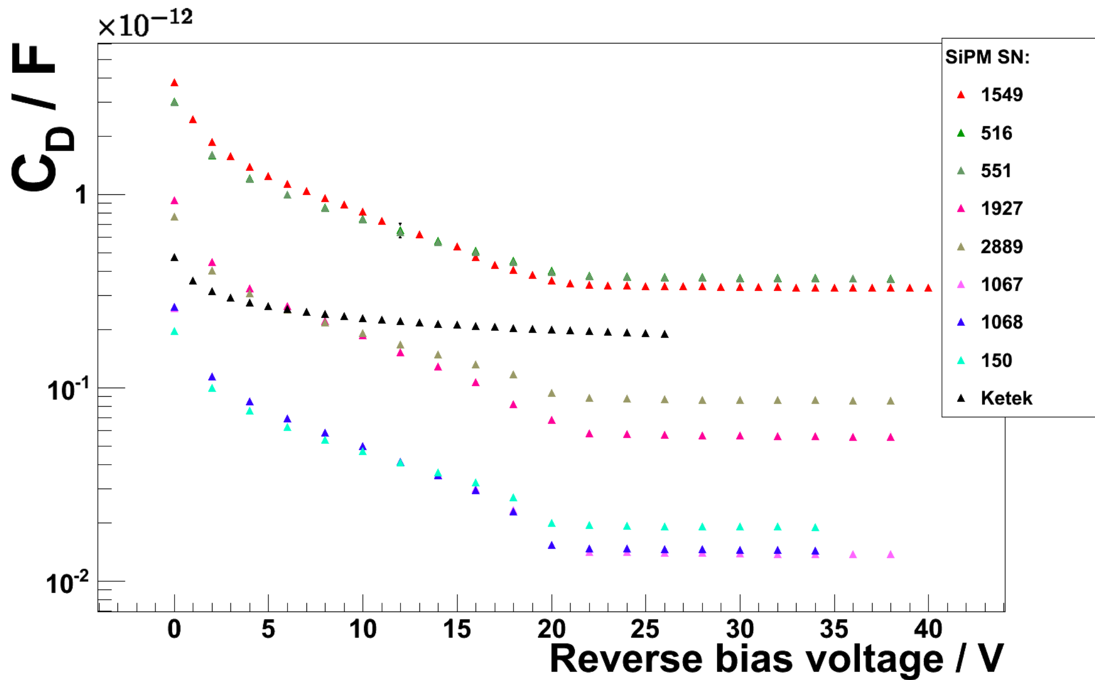

Figure 4.4: C_D at different reverse bias voltages for all SiPMs

The Ketek SiPM shows a different behavior. The diode capacitance can only be measured up to the breakdown voltage. So the capacitance is measured from 0 V - 26 V. The Ketek SiPM seems not to get into full depletion before breakdown. The capacitance is higher than for the Hamamatsu SiPMs with 50 μm pixel size and 9 mm^2 detector size and thus it is expected that the Ketek SiPM has a higher recovery time. To determine the diode capacitance at the operating voltage for the Hamamatsu SiPMs a curve

$$f(V) = a + \frac{b}{\sqrt{c + \mathrm{V}}} \tag{4.4}$$

with V the applied voltage (corresponding to formula 2.5) is fitted to the data points at 30 V - 40 V and then extrapolated to a typical bias voltage of 72.5 V (cf. section 2.3). A systematic uncertainty is estimated by the variation of the capacitance between 70 V - 75 V and calculating

$$\sigma_{\mathrm{sys}} = \left| \frac{C_\mathrm{D}(75\,\mathrm{V}) - C_\mathrm{D}(70\,\mathrm{V})}{2} \right|. \tag{4.5}$$

The statistical uncertainty is the uncertainty on the value at 72.5 V that is gained from the fit with formula 4.4. This variation by 5 V covers the typical operating voltage range of Hamamatsu SiPMs. The Ketek SiPM's capacitance at breakdown is the value extrapolated to 28 V. All data is shown in table 4.2.

SN.	SiPM Size	Capacitance at breakdown / F
1549	1x1, 100	$(3.180 \pm 0.028(\mathrm{stat.}) \pm 0.005(\mathrm{sys.})) \cdot 10^{-13}$
516	3x3, 100	$(3.554 \pm 0.030 \pm 0.006) \cdot 10^{-13}$
551	3x3, 100	$(3.529 \pm 0.035 \pm 0.005) \cdot 10^{-13}$
1927	1x1, 50	$(5.323 \pm 0.043 \pm 0.010) \cdot 10^{-14}$
2889	3x3, 50	$(8.329 \pm 0.101 \pm .0011) \cdot 10^{-14}$
1067	1x1, 25	$(1.314 \pm 0.021 \pm 0.002) \cdot 10^{-14}$
1068	1x1, 25	$(1.357 \pm 0.018 \pm 0.003) \cdot 10^{-14}$
150	3x3, 25	$(1.842 \pm 0.011 \pm 0.002) \cdot 10^{-14}$
Ketek	3x3, 50	$(1.880 \pm 0.021 \pm 0.008) \cdot 10^{-13}$

Table 4.2: Extrapolated diode capacitance at operating voltage (72.5 V for Hamamatsu SiPMs, 28 V for the Ketek SiPM)

One would expect that the pixels with the same size have the same diode capacitance. But the SiPMs with the same pixel size have a larger diode capacitance for larger detector areas. Thus

the full depletion depth is larger for smaller detector areas. The full depletion depth is mainly driven by the thickness of the epitaxial layer. Due to that SiPMs with a smaller detector area seem to have a larger epitaxial layer that might be caused by production factors.

4.3.1 Depletion depth

An estimator for the depletion depth can be easily calculated by assuming the pixel size to be the area A of the parallel plate capacitor with

$$C_D = \epsilon_0 \epsilon_{Si} \frac{A}{d} \quad \Rightarrow \quad d = \epsilon_0 \epsilon_{Si} \frac{A}{C_D} . \tag{4.6}$$

The illustration of this calculation indicates that the SiPM is fully depleted at ~ 20 V (see figure 4.5). As stated before, the SiPM is operated at a higher voltage than the voltage of full depletion to gain a higher photon detection efficiency.

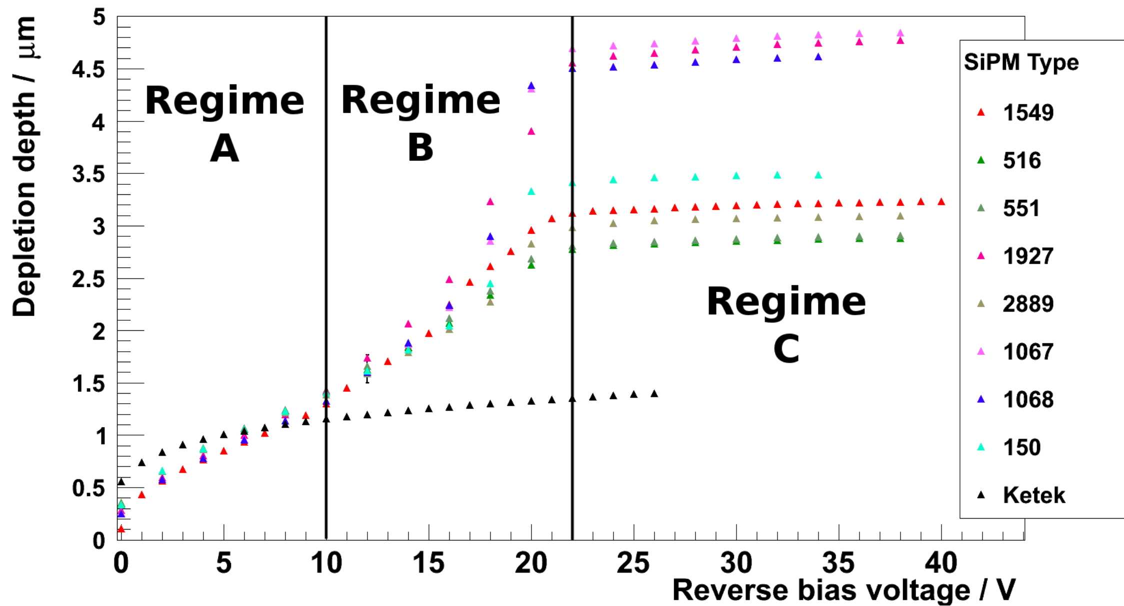

Figure 4.5: Depletion depth at different reverse bias voltages

The depletion of the Hamamatsu SiPMs can be divided into three regimes. The first regime (regime A, $(0 - 1.2)$ μm) can be associated with the first highly doped layer directly at the p-n-junction. In the second regime (regime B, $(1.5 - 2.5)$ μm), that has a doping concentration

approximately 3 to 24 times lower than the first regime, the d-V-curve shows a higher slope and can be related to the epitaxial layer since it is expected to have a lower doping density. The third regime (C) starts at about 3 μm or 4.5 μm, respectively, which corresponds to the substrate of the SiPM. The depletion almost comes to a stop with increasing reverse bias voltage.

As explained in the previous section the full depletion depth for 1 mm^2 SiPMs is larger ($\sim$ 4.5 μm) than for 9 mm^2 SiPMs ($\sim$ 3 μm). The epitaxial layer is not explicitly important for the SiPM's behavior and might thus underly large variations in the production. However, the larger epitaxial layer for smaller detector sizes might be helpful to gain a stable electric field in the SiPMs since the relative number of pixels at the SiPM's boundaries is higher for small detectors. And thus relatively more pixels are not surrounded uniformly by other pixels which can lead to a non-uniform electrical field in these boundary pixels that possibly could be fixed by a larger epitaxial layer.

The Ketek SiPM has a significantly smaller depletion depth at breakdown ($\sim$ 1.3 μm). This corresponds to the relatively high diode capacitance for the 50 μm pixel size SiPMs and the occurring breakdown before full depletion. The depletion depth of the Ketek SiPM does not show a certain structure. This points to a different doping structure compared to Hamamatsu SiPMs.

4.3.2 Doping

The doping concentration of the SiPM can be determined for the lower doped side of the p-n-junction with

$$N = -\left(\frac{d(1/C_\mathrm{D}^2)}{dV}\right)^{-1} \frac{2}{q\epsilon_0\epsilon_\mathrm{Si}A^2} \tag{4.7}$$

with $q = 1.602\cdot10^{-19}$ C (cf. equation 2.10). Please note that $V < 0$ for reverse bias voltage. The $1/C_\mathrm{D}^2$-V curve shows the three located regimes even more clearly. By determination of the slope in these three regimes the doping concentration for n-doped layers can be found (see figure 4.6).

The measured doping concentrations for all SiPMs is shown in table 4.3.

The doping concentration in the first regime varies by 18% between the different Hamamatsu SiPM types. This regime is crucial for the p-n-junction and the gain of the SiPM. To achieve comparable results for the amplification it is important that the doping in this regime is the same for the different SiPM types. Note that the errors are statistical errors for the fit and do

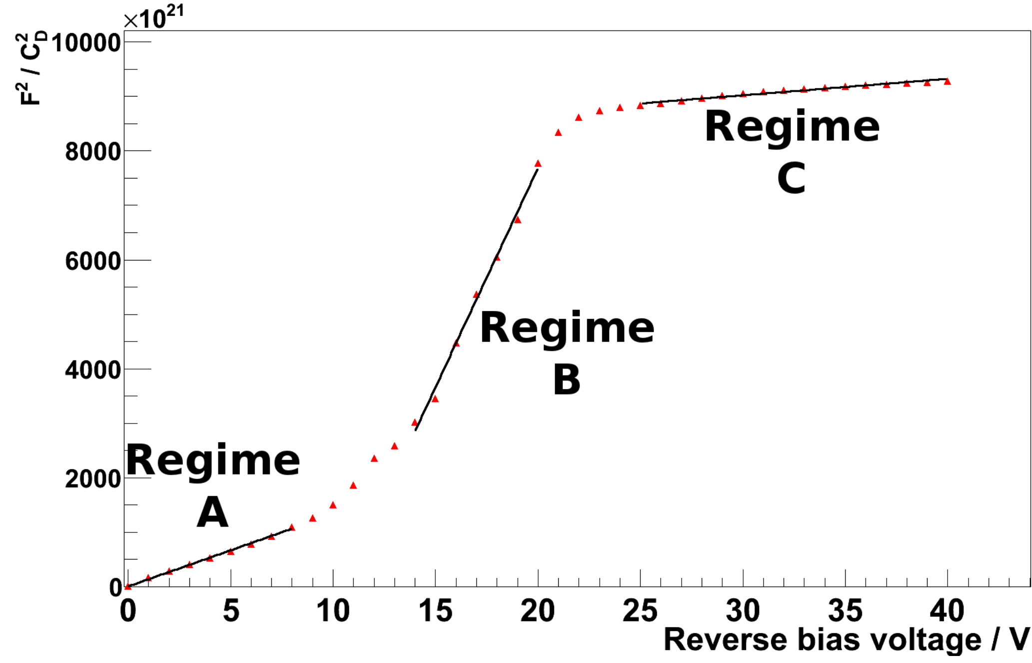

Figure 4.6: $1/C_D^2$-V curve and fits for the Hamamatsu SiPM 516; the three regimes are marked, the transition regions between these regimes are clearly visible

Serial No.	Type	Doping concentration / cm^3		
		Regime A	Regime B	Regime C
		n^+-region	epitaxial layer	wafer
1549	1x1,100	$(8.837 \pm 0.031) \cdot 10^{15}$	$(1.458 \pm 0.016) \cdot 10^{15}$	$(38.879 \pm 0.016) \cdot 10^{15}$
516	3x3, 100	$(6.899 \pm 0.032) \cdot 10^{15}$	$(2.239 \pm 0.043) \cdot 10^{15}$	$(52.278 \pm 0.042) \cdot 10^{15}$
551	3x3, 100	$(6.824 \pm 0.031) \cdot 10^{15}$	$(2.139 \pm 0.021) \cdot 10^{15}$	$(50.273 \pm 0.021) \cdot 10^{15}$
1927	1x1, 50	$(7.572 \pm 0.035) \cdot 10^{15}$	$(0.689 \pm 0.008) \cdot 10^{15}$	$(13.222 \pm 0.008) \cdot 10^{15}$
2889	3x3, 50	$(7.120 \pm 0.033) \cdot 10^{15}$	$(1.571 \pm 0.017) \cdot 10^{15}$	$(54.094 \pm 0.017) \cdot 10^{15}$
1067	1x1, 25	$(8.343 \pm 0.038) \cdot 10^{15}$	$(0.355 \pm 0.009) \cdot 10^{15}$	$(14.677 \pm 0.009) \cdot 10^{15}$
1068	1x1, 25	$(8.366 \pm 0.038) \cdot 10^{15}$	$(0.353 \pm 0.006) \cdot 10^{15}$	$(13.729 \pm 0.006) \cdot 10^{15}$
150	3x3, 25	$(6.943 \pm 0.032) \cdot 10^{15}$	$(0.715 \pm 0.018) \cdot 10^{15}$	$(50.509 \pm 0.018) \cdot 10^{15}$

Table 4.3: Doping concentration in three different regimes

not include the systematics of this measurement method that assumes an abrupt junction. To gain information about the systematic uncertainties it is helpful to use the values for the SiPMs with the serial numbers 1067 and 1068. These SiPMs with adjacent serial numbers were very likely produced on the same wafer. Therefore, it is expected that these SiPMs have almost the same values for the doping concentration in the three regions. For the regimes A and B the systematic uncertainties are smaller than the statistical ones and thus neglected.
The doping of the epitaxial layer (Regime B) shows a systematic behavior. SiPMs with a smaller pixel size have a smaller doping in this region. But SiPMs with larger detector area have a higher doping in the epitaxial layer. Though the epitaxial layer has no direct influence on the G-APD's function, it might be used to create a more homogeneous electric field within the p-n-junction. So for smaller pixel sizes it might be feasible to gain a larger depletion depth since the influence of the boundary effects are increasing and a larger depletion depth can help to stabilize the electric field.
The regime C represents the wafer. The doping of the wafer is not important for the SiPM itself. It is only important to have the same doping type as the epitaxial layer to avoid another p-n-junction. The doping concentration is high compared to the other layers, but still small compared to other usual doping concentrations in semi-conductor devices which can be $\sim 10^{-19} \frac{1}{\text{cm}^3}$. A systematic uncertainty can be estimated with $0.5 \cdot 10^{15} \frac{1}{\text{cm}^3}$ by comparing SiPMs 1067 and 1068 and calculating

$$\sigma_{\text{sys}} = \frac{N_{1067} - N_{1068}}{2} \tag{4.8}$$

with N the doping concentration. The systematic uncertainty is not negligible in this regime anymore because the approximation of a single-sided abrupt junction is getting worse with varying doping profiles. Because of the unimportance of the doping concentration of the wafer, the different measurement values can be explained with different wafers used for the SiPM production.

4.4 Results for C_Q

The quenching capacitance was fixed after the first fit to the impedance curve. So the value of the quenching capacitance is assumed to be independent of the reverse bias voltage. The measured values for all SiPMs are shown in table 4.4 and figure 4.7.
All values for the quenching capacitance are of the same order of magnitude ($\sim$ 100 nF). Since

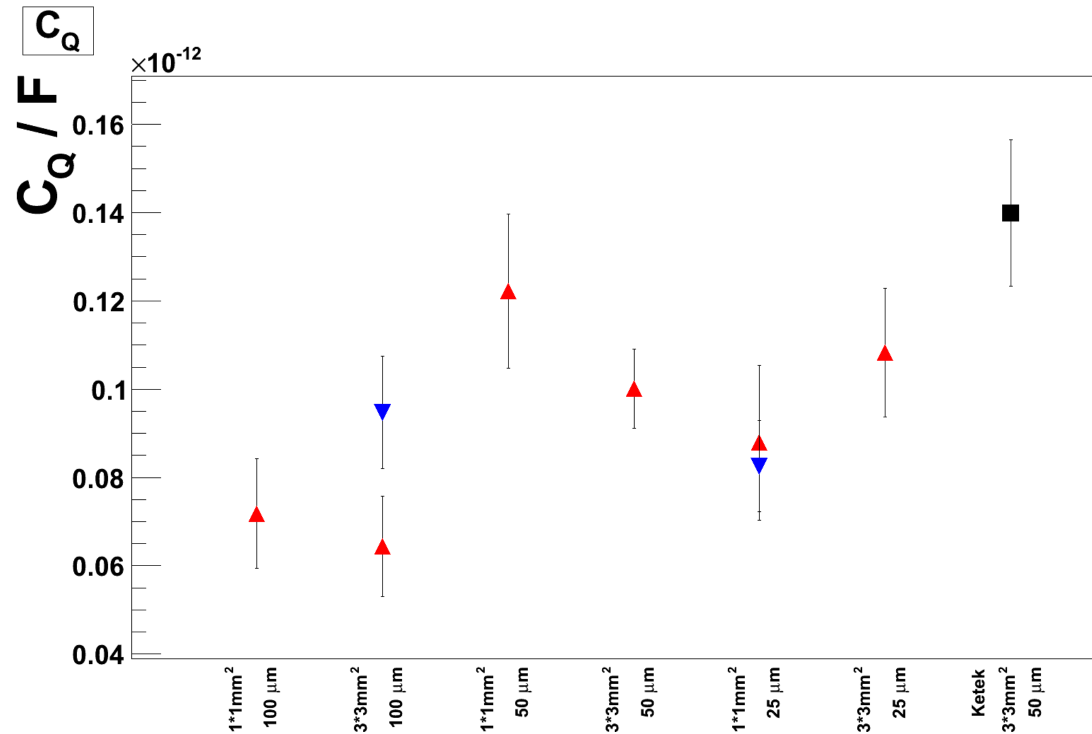

Figure 4.7: Measured C_Q values, (Black square: Ketek SiPM, Triangles: Hamamatsu SiPMs)

the quenching capacitance is a parasitic effect, it is expected that the manufacturers try to reduce this value and thus do not try to get well defined non-zero quenching capacitances. So variations in the quenching capacitance are mainly due to the production process and pixel to pixel variations.

The measured values are comparable with the measurements of other groups though they tested SiPMs from different manufacturers (21.2 fF, 12.2 fF in [29]). Since the values are all in the same order of magnitude for many different manufacturers, these quenching capacitances currently seem to be the best achievable result for the quenching capacitance using a quenching resistor on top of the G-APD surface.

The data shows no systematic behavior regarding the pixel and detector size. The Ketek SiPM has a slightly higher quenching capacitance but the value is comparable with the Hamamatsu SiPMs within uncertainties.

The relatively high uncertainty on the measured values (10% - 15%) can be a hint that the variation of the quenching capacitance has a less significant impact on the impedance values

SN.	SiPM size	Quenching Capacitance / fF	Number of pixels
1549	1x1,100	71.8 ± 12.5	100
516	3x3,100	64.4 ± 11.4	900
551	3x3,100	94.6 ± 12.7	900
1927	1x1,50	122.2 ± 17.5	400
2889	3x3,50	100.1 ± 9.0	3600
1067	1x1,25	87.9 ± 17.5	1600
1068	1x1,25	82.6 ± 10.4	1600
150	3x3,100	108.4 ± 14.6	14400
Ketek	3x3,50	139.9 ± 16.6	3600

Table 4.4: Results for the quenching capacitance for all SiPMs, the uncertainties are also gained from the fit of the impedance formula to the data (cf. section 4.2)

compared to the quenching resistor. A comparison of the quenching resistor's impedance

$$Z_{R_Q} = R_Q = (118.1 \pm 0.3)\ \mathrm{k\Omega} \tag{4.9}$$

with the quenching capacitance's impedance at 2 MHz

$$Z_{C_Q} = \frac{1}{2\pi f C_Q} = (1109.1 \pm 192.9)\ \mathrm{k\Omega} \tag{4.10}$$

for the Hamamatsu SiPM 1549 shows that the quenching resistance has a ten times greater impact on the impedance of the parallel circuit of quenching resistor and capacitance. For lower frequencies this factor increases $\propto C_Q$. Thus only impedance values at high frequencies carry information about the quenching capacitance. This causes the relatively large error on the capacitance values compared to the diode capacitance and the quenching resistance. Consequently, measurements with a higher frequency are needed to determine the quenching capacitance more accurately. At a frequency of about 20 MHz the impedance of the quenching capacitance and the quenching resistor are in the same order of magnitude. At this frequency a precise measurement of the quenching capacitance is expected to be possible. Measurements at higher frequencies than 2 MHz were not taken because the used measurement device is not capable of using these test frequencies.

4.5 Results for C_G

The measured grid capacitance is shown in table 4.5 and figure 4.8.

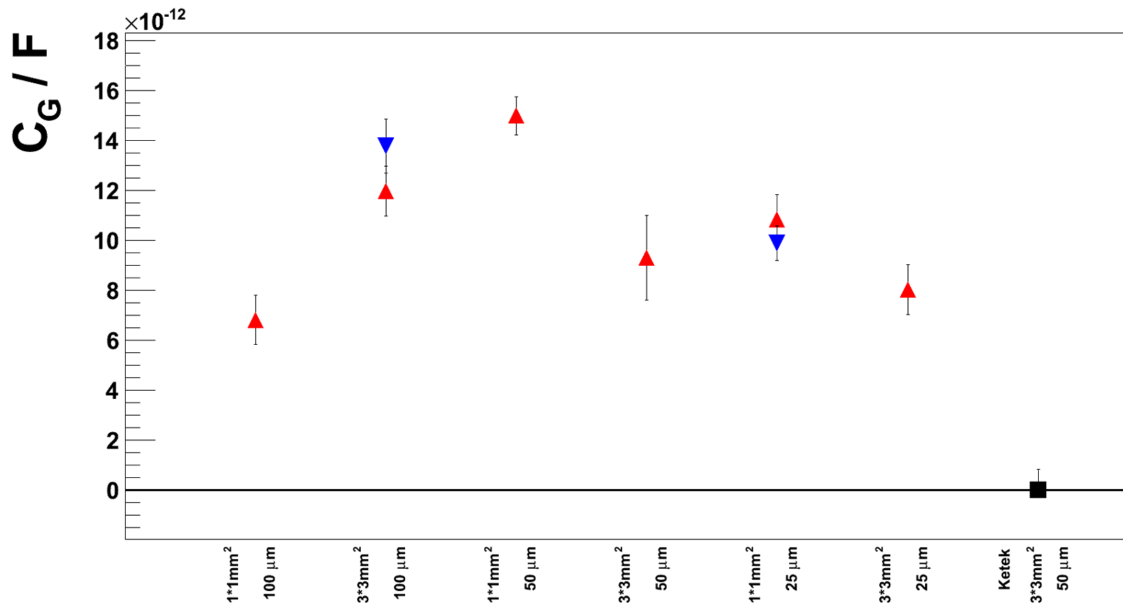

Figure 4.8: Measured grid capacitances C_G, (Black square: Ketek SiPM, Triangles: Hamamatsu SiPMs)

This parameter absorbs all other parasitic effects of the SiPM. This includes the connection pins and wafer effects. A systematic pattern is not obvious in the data. The Ketek SiPM has no grid capacitance within uncertainties. Since the macroscopic connection pins should have a similar capacitive behavior for all tested SiPM types, it is likely that the grid capacitance is unaffected by the pins but rather driven by the connection between the pins and the wafer and the wafer itself.
All values for the grid capacitance of the Hamamatsu SiPMs are in the same order of magnitude. For identical SiPM types the values match within the uncertainties.
The grid capacitance itself will not have a deep impact on the pulse shape because it is par-

SN.	SiPM size	Grid Capacitance / pF	Number of pixels
1549	1x1,100	6.81 ± 0.99	100
516	3x3,100	11.98 ± 1.07	900
551	3x3,100	13.78 ± 1.09	900
1927	1x1,50	15.00 ± 0.77	400
2889	3x3,50	9.31 ± 1.70	3600
1067	1x1,25	10.85 ± 0.98	1600
1068	1x1,25	9.89 ± 0.69	1600
150	3x3,25	8.03 ± 1.00	14400
Ketek	1x1,50	$0.00^{+0.82}_{-0.00}$	3600

Table 4.5: Results for the grid capacitance for all SiPMs, the uncertainties are gained from the fit of the impedance formula to the data (cf. section 4.2)

allel to the whole SiPM and likewise parallel to the connected voltage source. Thus the grid capacitance behaves like an additional capacitance of the voltage source and readout electronics (see section 6.7).

5 Recovery Time

5.1 Determination of the recovery time from electrical parameters

The decay constant of the falling tail of an SiPM single pixel pulse is called recovery time (τ_{rec}, see also figure 5.1).
The recovery time of an SiPM is directly related to its electrical properties. In a first approximation the diode acts as charged capacitor. If a breakdown occurs, the diode is discharged via the quenching resistor. So the recovery time is in the same order of the RC time constant [25]

$$\tau = R_{\mathrm{Q}} \cdot C_{\mathrm{D}} \ . \tag{5.1}$$

The recovery time τ for the recharge of the diode capacitance

$$U_{\mathrm{C}}(t) = U_{\mathrm{C}_0} \left(1 - \exp\left(-\frac{t}{R_{\mathrm{Q}} \cdot C_{\mathrm{D}}} \right) \right) \tag{5.2}$$

serves as a good crosscheck to see if the values for R_{Q} and C_{D} are within a reliable range.
The values of R_{Q} and C_{D} have been measured (see sections 4.1 and 4.3). The resulting time constants are shown in table 5.1. For the diode capacitances the values at breakdown are used. Though SiPMs are operated a few volts above the breakdown voltage, this is a sufficient approximation due to the small diode capacitance variation at high reverse bias voltages (see section 4.2).
As expected, the recovery time decreases with decreasing pixel size. The Ketek SiPM has a significantly higher recovery time. This result coincides with the measurements reported in [9].

5.2 Determination of the recovery time from dark noise

To compare the derived recovery time, the recovery time is also measured from the signal shape of the SiPM dark noise. Therefore, an SiPM dark noise signal trace is recorded and an

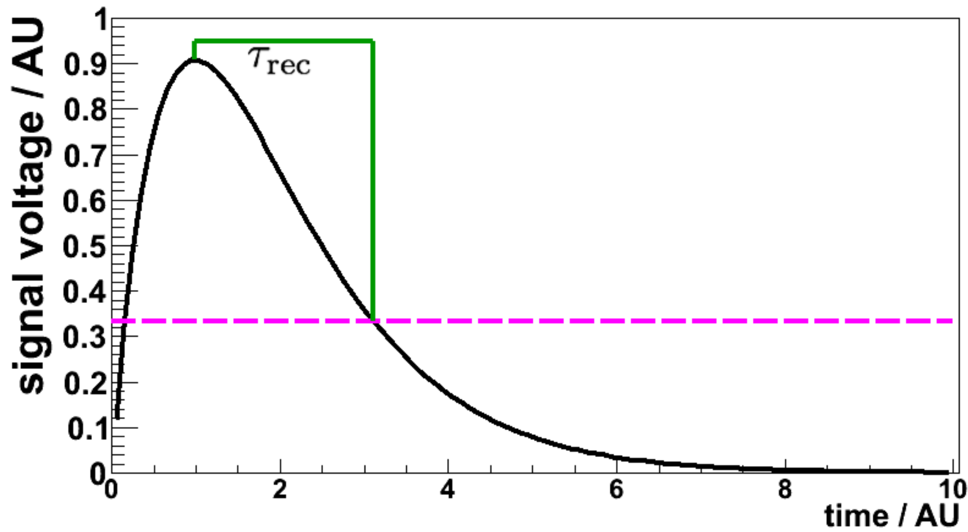

Figure 5.1: Scheme of an SiPM pulse, dashed line: $\frac{1}{e}$ of the maximum signal height; green: time constant of this pulse

SN.	SiPM size	R_Q / kΩ	C_D / F	Time Contant / ns
1549	1x1,100	118.1 ± 0.3	$(3.180 \pm 0.005) \cdot 10^{-13}$	37.56 ± 0.12
516	3x3,100	122.9 ± 0.3	$(3.554 \pm 0.006) \cdot 10^{-13}$	43.68 ± 0.13
551	3x3,100	119.7 ± 0.3	$(3.529 \pm 0.005) \cdot 10^{-13}$	42.24 ± 0.12
1927	1x1,50	128.7 ± 0.4	$(5.323 \pm 0.010) \cdot 10^{-14}$	6.85 ± 0.03
2889	3x3,50	151.2 ± 0.4	$(8.329 \pm .0011) \cdot 10^{-14}$	12.59 ± 0.04
1067	1x1,25	275.5 ± 0.8	$(1.314 \pm 0.002) \cdot 10^{-14}$	3.62 ± 0.01
1068	1x1,25	274.9 ± 0.8	$(1.357 \pm 0.003) \cdot 10^{-14}$	3.73 ± 0.03
150	3x3,25	337.1 ± 0.9	$(1.842 \pm 0.002) \cdot 10^{-14}$	6.21 ± 0.02
Ketek	3x3,50	375.1 ± 1.1	$(1.880 \pm 0.008) \cdot 10^{-13}$	70.05 ± 0.36

Table 5.1: Resulting time constant $\tau = R \cdot C$ for all SiPMs

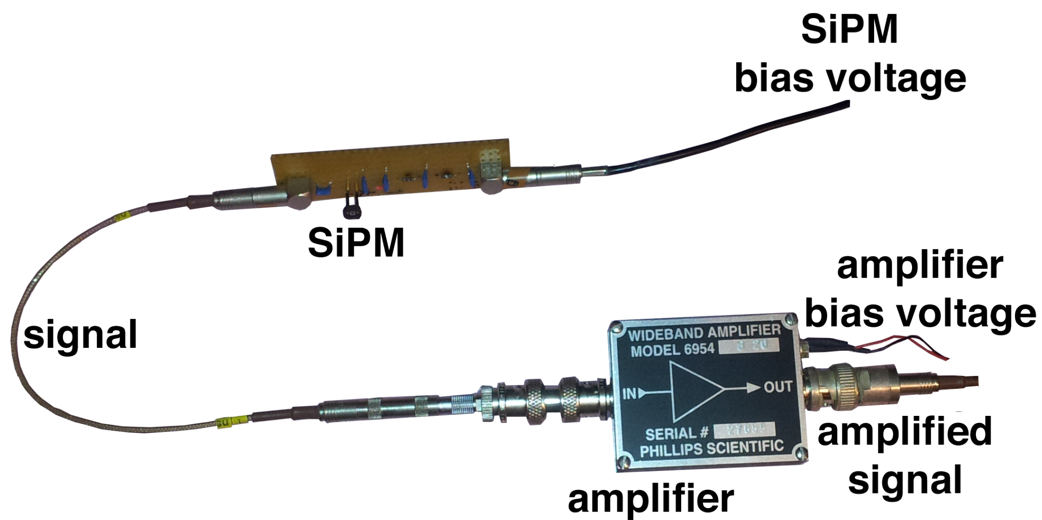

Figure 5.2: Picture of parts of the setup for recovery time determination via oscilloscope

exponential function is fitted to every tail of an SiPM pulse. The time constant is extracted from these fits.

5.2.1 Setup

The setup for direct recovery time estimation from the SiPM's noise consists of two DC-power supplies, a connection board for the SiPM, an amplifier board and an oscilloscope. The SiPM bias voltage is directed to the connection board. The output signal is then amplified by the wide-band amplifier that is connected to the second power supply. This amplified signal is now transferred to the oscilloscope by a LEMO cable. The data can be recorded via an USB data storage and brought to a PC where it is analyzed. The SiPM and the amplification board are placed inside a metal dark box to avoid light-induced SiPM signals and insulate the devices from external electromagnetic noise. For a picture of the connection board and the amplifier see figure 5.2. For a schematic view of this setup see figure 5.3.

5.2.1.1 SiPM power supply

The SiPM power supply is provided by the EA-PSI 6150-01 power supply. This device can supply a bias voltage from 0 V - 150 V with a resolution of 10 mV. The accuracy is 0.05% at 25 °C operating temperature with a stability of < 5 mV over the whole voltage range and a ripple of < 3 mV [32]. The supply voltage is always set to the recommended operating voltage given by the SiPMs manufacturer at 25 °C.

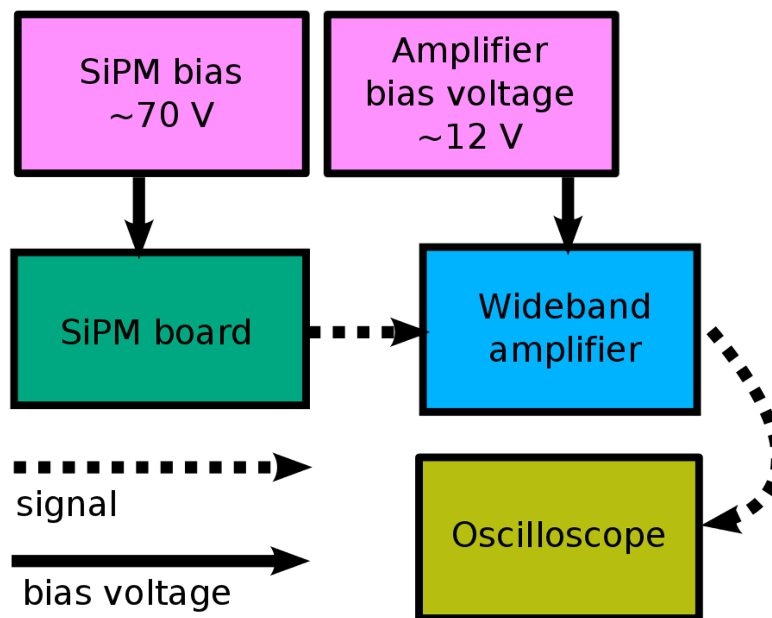

Figure 5.3: Sketch of setup for recovery time determination via oscilloscope

5.2.1.2 Connection board

The connection board is a combination of a π-filter and readout electronics that is suggested by Hamamatsu data sheets [16]. The π-filter consists of two resistors (100 Ω, 220 Ω) and three 100 nF capacitors, one in front of the first resistor, one in the middle between the first and second resistor and one behind the second resistor. All capacitors are connected to ground (see figure 5.4). This filter reduces possible noise from the SiPM bias voltage source.
The second part of the board is the readout electronics that is suggested by Hamamatsu in their data sheets [16]. The electronics decouples the signal via an 100 nF capacitor and ter-

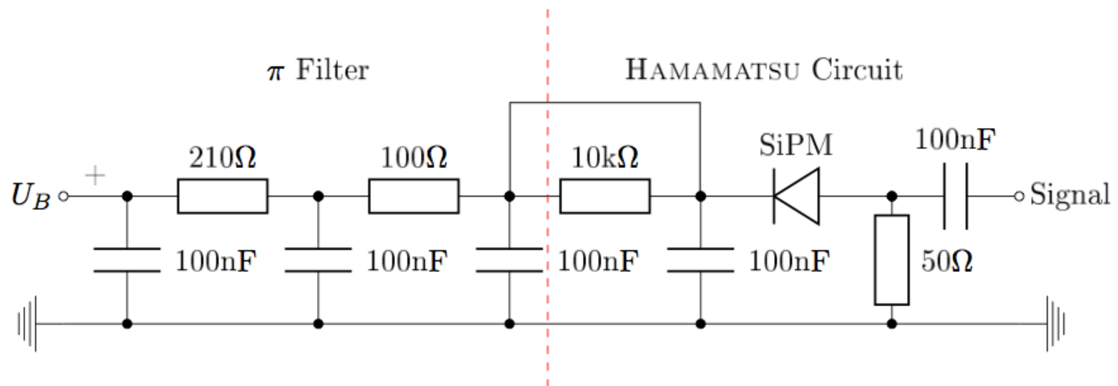

Figure 5.4: Circuit of the connection board [9, Slightly modified]

minates the signal with 50 Ω. The 10 kΩ resistor was later bypassed with a wire because it became obvious that this resistor changed the shape of the SiPM pulse considerably [33].

5.2.1.3 Amplifier

The amplifier is a Phillips scientific wide band amplifier (model 6954) with a voltage amplification factor of 20. The amplifier has a nominal bandwidth from 100 kHz to 1.5 GHz [34]. A measurement of the gain with a FSH4 - 100047/024 spectrum analyzer by Rhode & Schwarz [35] is shown in figure 5.5. The gain is not flat above 500 MHz anymore but drops slightly below the 3dB level that defines the bandwidth and rises above 750 MHz again.
The amplifier needs a nominal bias voltage between 10 V and 28 V. If it is operated above 24 V a heat sink is recommended [34]. In this setup the amplifier is biased with 12 V since this results in a slightly better performance than with 10 V bias (see figure 5.5) in the frequency range between 1.0 GHz - 1.7 GHz.

5.2.1.4 Amplifier bias voltage source

The 12 V bias voltage for the amplifier operation is provided by an EA-PS 2000 voltage supply. It has a stability of < 50 mV and a ripple of < 4 mV. It can output voltages between 0 V and 16 V [36]. So this device is feasible as amplifier bias because the amplifier works in the whole range from 10 V to the maximum output of 16 V (see section 5.2.1.3).

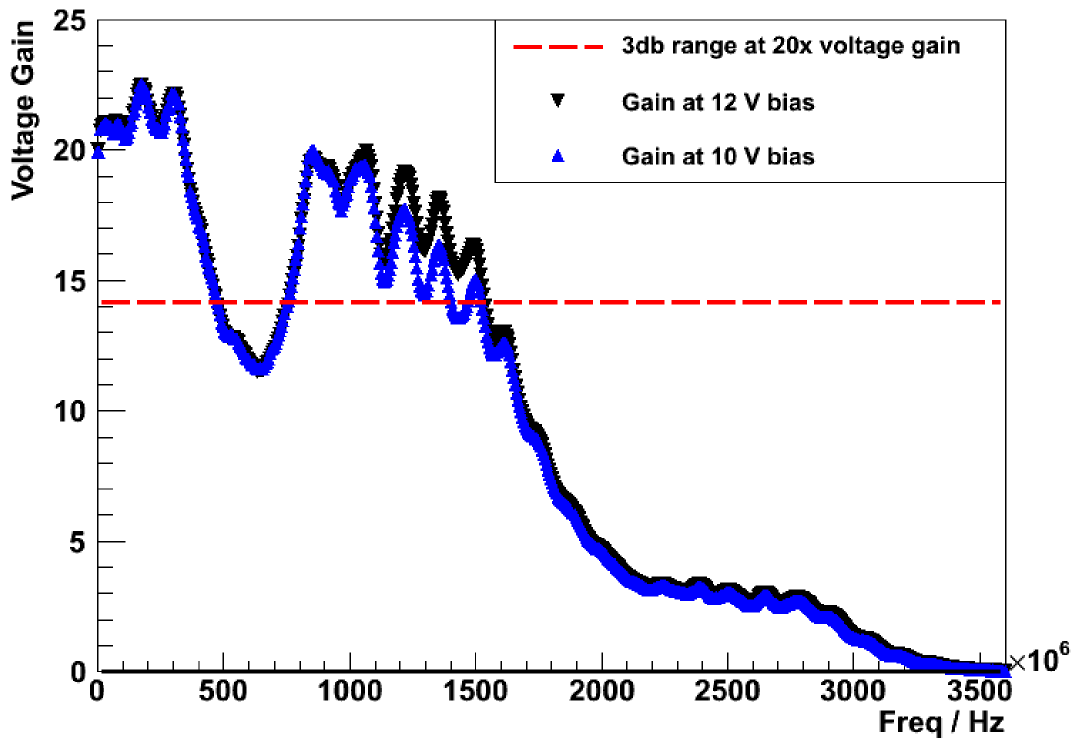

Figure 5.5: Amplification measurement of the Phillips scientific amplifier with a R & S FSH4 spectrum analyzer

5.2.1.5 Oscilloscope

The used oscilloscope is a 4-channel DPO 7104 by Tektronix [37]. It has a 1 GHz bandwidth and can take 50,000,000 data points in 20 ms corresponding to a time step of 400 ps. It is operated with an input impedance of $(50.0 \pm 0.1)\ \Omega$ and has a parallel capacitance of (13 ± 2) pF. The random noise of this device for the used voltage step of 2 mV is 0.135 mV and can be assumed as error on the measured values.
All data is stored on a USB data storage in the .xls format and can be processed by a PC.

5.2.2 Measurement and results

In a first step the whole recorded signal trace is flattened with a moving average

$$V(t_i) = \frac{\sum_{j=i-2}^{i+2} V(t_j)}{5} \tag{5.3}$$

with t_i the i-th time step in the signal. So the moving average is calculated over $\Delta t \cdot 5 = 2$ ns. With this method the distortions by the oscilloscope are reduced. On the other hand, edges shorter than 2 ns are stretched, which corresponds to a cutoff frequency of 500 MHz. This, however, does not affect the measurement results since the amplifier has a homogeneous amplification up to 500 MHz (see section 5.2.1.3).
After this step the first discrete derivative

$$\frac{dV(t_i)}{dt} = \frac{V(t_{i-1}) - V(t_{i+1})}{3} \tag{5.4}$$

(for $i = 2 ... n-2$) of the signal is calculated. This derivative is more sensitive to fast signal variations because steep edges in the signal result in very high derivative values. By setting a threshold on these derivative values the peaks can then be identified. Graphs of a part of a signal trace before and after the described steps are shown in figure 5.6.
To find the peaks within the signal the signal trace is scanned from the beginning. If the derivative exceeds a certain value, that is adjusted for every SiPM, the maximum of the following 5 ns is defined as the peak's maximum. For a dead time of 10 ns no second peak is recognized. To determine the recovery time clean single pulses are needed. To filter for these pulses only peaks without another peak 200 ns before and afterwards are selected.
All peaks are then analyzed. The recovery time is determined as the exponential time constant from an exponential fit to the tail of the SiPM pulse. This is closely connected to the definition of the recovery time as $\tau = R \cdot C$ from the electrical parameters since the value τ is the time constant of the exponential discharge of an RC-chain (see section 5.1).
The determined time constants are filled into a histogram. This histogram yields the mean and the error on the mean for this time constant for a specific SiPM (see figure 5.7). The results for this determination are shown in table 5.2.
All results of the recovery time determination are shown in figure 5.8. The measured results from [9] are also included. This data was taken from SiPMs that were fully illuminated.
The data points are in good agreement with each other. The recovery time decreases with

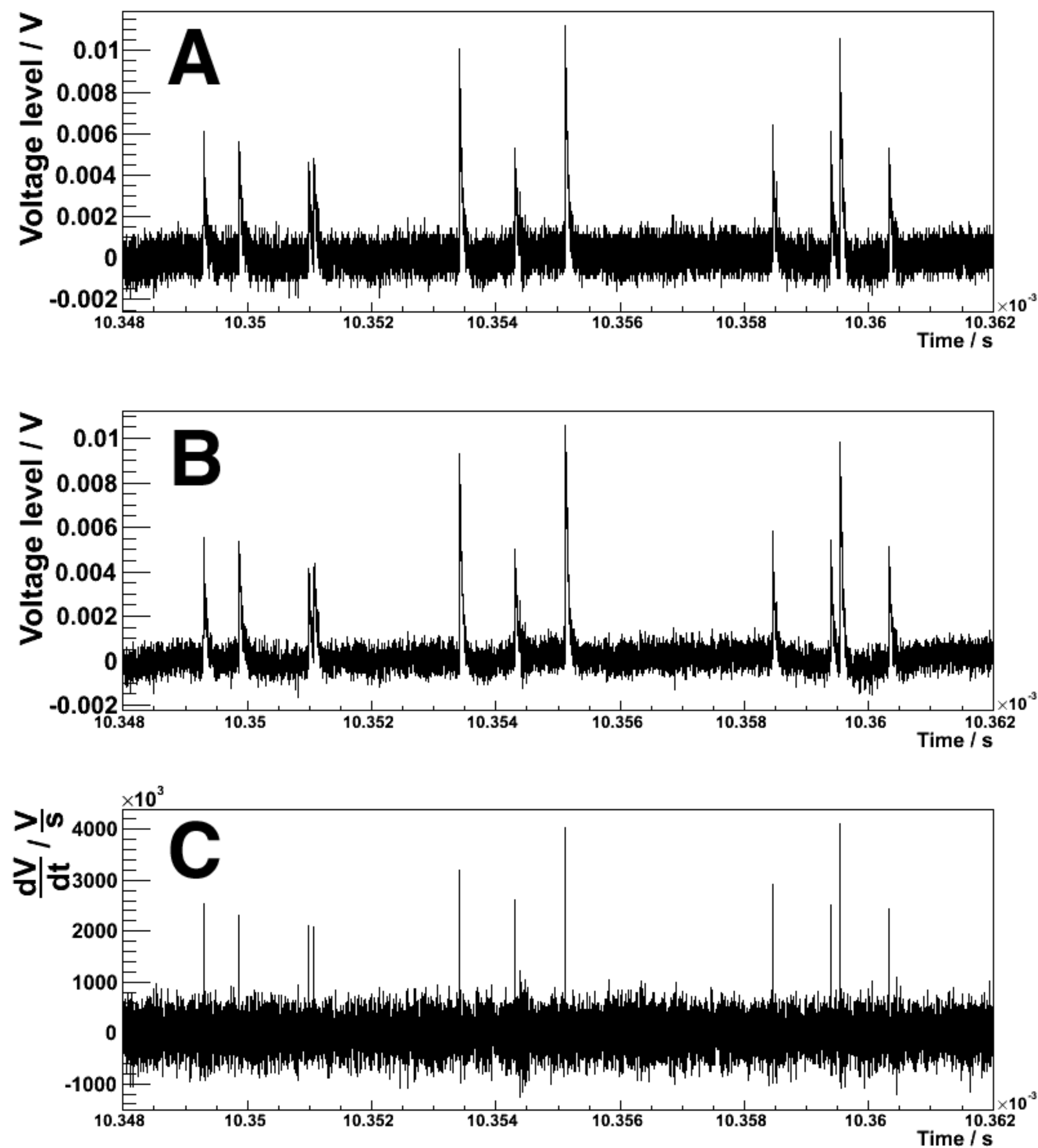

Figure 5.6: A) Part of an unprocessed voltage trace; B) Part of a flattened voltage trace (the reduction of the noise-level can be seen best in the baseline); C) Part of the derivative of a voltage trace (the peaks at the beginning of the pulses are clearly visible; the negative peaks at the falling edge of the pulses are too small to be visible because the falling edge is less steep then the rising edge); for an illustration of the data processing steps at one single pixel see figure A.5 in the appendix

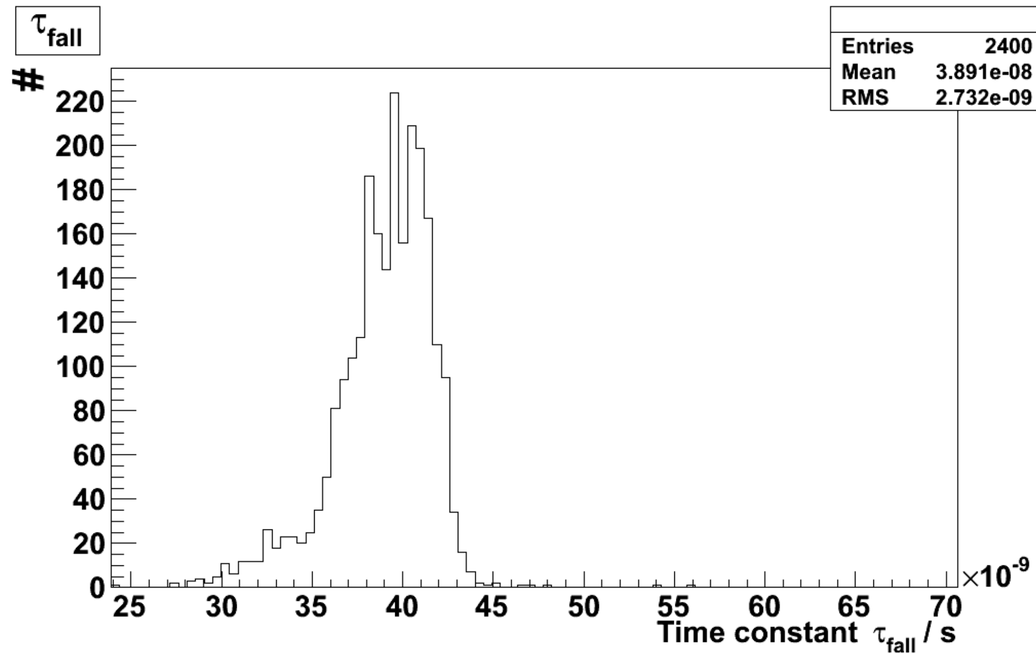

Figure 5.7: Histogram of measured recovery time constants (τ) for the Hamamatsu SiPM SN: 1549 (1x1,100)

decreasing pixel size. A larger detector size yields a slightly larger recovery time. Only the recovery times for the Ketek SiPM vary by about 20% between the different measurement methods. This can be caused by the signal shape of the SiPM at full illumination [9] that differs from the shape of the Hamamatsu SiPMs and does not allow a perfect exponential fit to the tail of the signal.

All in all, the good agreement of the measurements of the recovery time indicate a good measurement of the two most important parameters (R_Q and C_D).

This setup also allows for the measurement of other parameters such as the crosstalk probability and the afterpulsing probability. However, this is not presented in this work because these values are not related to the electrical properties of the SiPMs.

SN.	SiPM size	Time Constant τ_{trace} / ns	Time Constant τ_{el} / ns
1549	1x1,100	38.91 ± 2.73	37.56 ± 0.12
516	3x3,100	43.34 ± 3.10	43.68 ± 0.13
551	3x3,100	43.91 ± 2.49	42.24 ± 0.12
1927	1x1,50	12.87 ± 1.94	6.85 ± 0.03
2889	3x3,50	16.72 ± 2.00	12.59 ± 0.04
1067	1x1,25	3.99 ± 0.51	3.62 ± 0.01
1068	1x1,25	5.71 ± 0.43	3.73 ± 0.03
150	3x3,25	8.53 ± 0.57	6.21 ± 0.02
Ketek	3x3,50	82.11 ± 5.22	70.05 ± 0.36

Table 5.2: Recovery time constant determined from the dark noise signal trace (τ_{trace}) and electrical parameters (τ_{el}, cf. table 5.1)

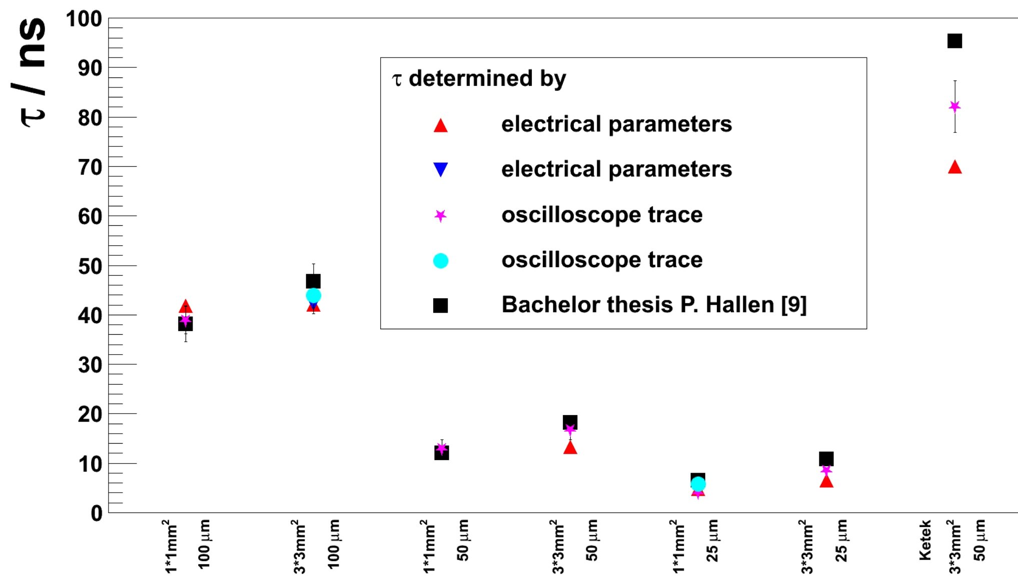

Figure 5.8: All measured and derived SiPM recovery time constants τ

6 SiPM Simulation

6.1 Electrical Simulations with Spice

Spice (Simulation Program with Integrated Circuit Emphasis) is a computer program for simulation of analogue and digital circuits. Originally it was developed at the University of California at the Institute for Electrical Engineering and Computer Sciences [38]. Many commercial and non-commercial programs implement this software for own simulation purposes.
Spice uses a net list of simple electrical devices that represents the connection between them. Using this list Spice computes an estimation for the behavior of the simulated circuit.
For purposes of this thesis the software LTSpice was used. LTSpice is developed by Linear Technology and under proprietary license. It uses Spice for the circuit calculations and provides a graphical user interface to implement the electrical devices.

6.2 Simulations with the SiPM model

Two different types of simulations were conducted. First the simulation with the originally discussed model and parameters (cf. 4) is shown. In a second step the model parameter (C_G) is varied due to deficits in the resulting pulse shape (see section 6.7).

6.2.1 Implementation of the initial model

To simulate the model discussed in section 2.4 a few variations have to be performed.
A voltage controlled resistance is placed in parallel to the diode capacitance. This device simulates the avalanche breakdown and thus has not been considered in the model yet because the extraction of the electrical parameters of this model was conducted with data that was taken at reverse bias voltages which did not allow an avalanche breakdown. This resistance has a value of $R_{\text{off}} = 385\ \text{G}\Omega$ if the pixel has currently no breakdown. This value is adapted from [30] and simulates a small dark current in the pixel. Moreover, the resistance value can not be set to infinity for simulation reasons. Variations of this value $> 1\ \text{G}\Omega$ did have no impact on the simulation results. In case of an avalanche breakdown this resistance value

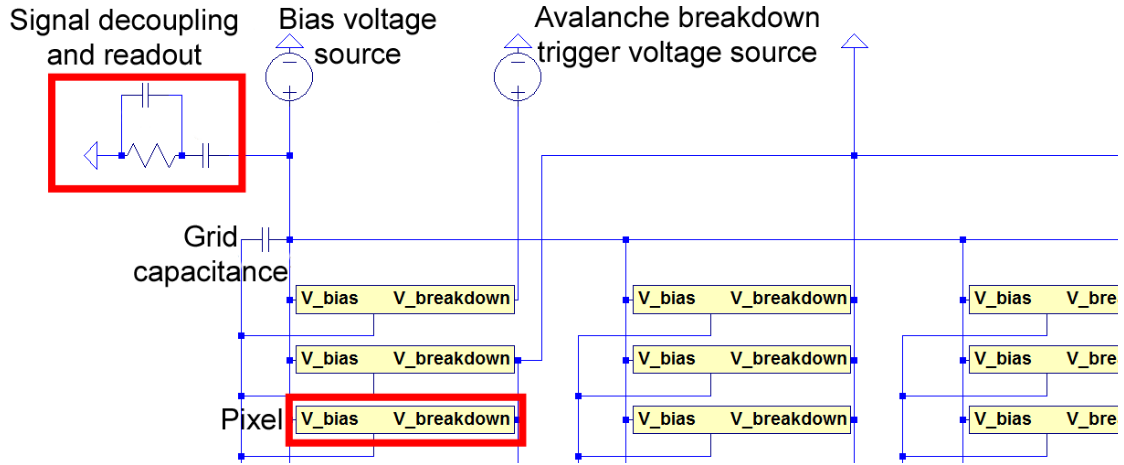

Figure 6.1: Screen capture of a typical LTSpice input; the yellow boxes represent pixels of the SiPM (cf. figure 6.2); pixels that do not fire a signal are grounded at the "V_breakdown" port; the upper left pixel is fired via the "Avalanche breakdown trigger source"

(R_{on}) is set to a certain value such that the diode capacitance is discharged during the time of breakdown O(1 ps) for

$$t_{\text{breakdown}} \approx 5 \cdot \tau = 5 \cdot R_{\text{on}} \cdot C_{\text{D}} \Rightarrow R_{\text{on}} \approx \frac{t_{\text{breakdown}}}{5 \cdot C_{\text{D}}} \tag{6.1}$$

A rough estimation for the breakdown duration is derived from the applied electric field

$$E = \frac{U_{\text{applied}}}{d} \approx \frac{70\ \text{V}}{4\ \mu\text{m}} \approx 17.5 \cdot 10^{4}\ \frac{\text{V}}{\text{cm}} \tag{6.2}$$

with $d \approx 4\ \mu$m the approximate thickness of the p-n-junction and the epitaxial layer, and the resulting mobility [2, p. 317, fig. 13]

$$\mu \approx 600\ \frac{\text{cm}^2}{\text{V} \cdot \text{s}} \tag{6.3}$$

that results in a time for the drift through the depleted region of

$$t_{\text{breakdown}} = \frac{d_{\text{amp}}}{v} = \frac{1\ \mu\text{m}}{v} = \frac{E \cdot \mu}{d} \approx 1\ \text{ps} \tag{6.4}$$

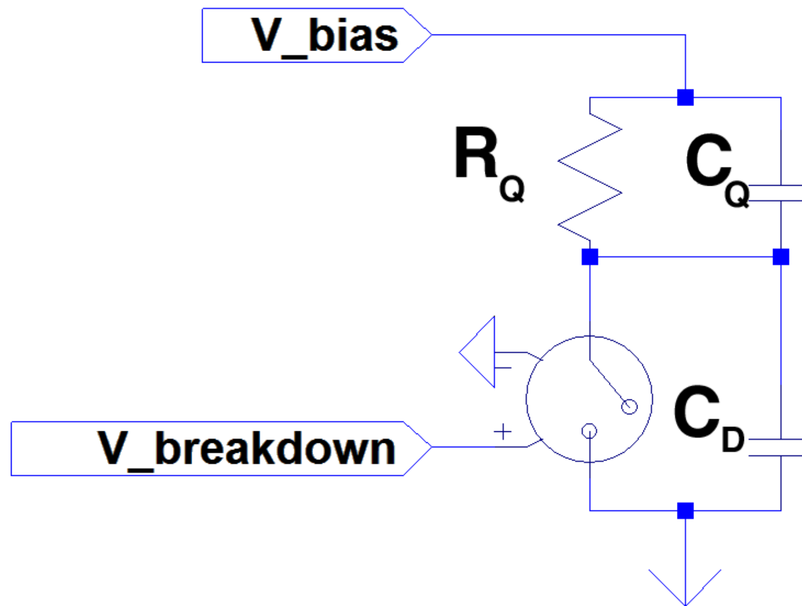

Figure 6.2: Screen capture of the LTSpice input for a single pixel

with the velocity v and $d_{\mathrm{amp}} \approx 1\ \mu$m the thickness of the charge carrier amplification region. Since it showed that the resulting pulse form is not affected by varying avalanche breakdown durations $t <\sim 100$ ps, this estimation is sufficient for the breakdown simulation.
The resulting resistance value for the variable resistor during breakdown is then calculated from the measured values of the diode capacitance using eq. 6.1. The values are shown in table 6.1. Using these values a full discharge of the diode capacitance is assured while the discharge of the grid capacitance via the quenching resistor is kept as small as possible. The advantage of using a voltage controlled resistance is that the avalanche breakdown can be triggered for every SiPM pixel discretely by applying an external voltage.
The second change in the model for simulations regards the signal readout. The SiPM is grounded via a 50 Ω resistor. The signal itself is decoupled with a 100 nF capacitor. These two changes are due to the read out board that is used to record SiPM pulses (see section 5.2.1.5). The decoupled signal is then read out at a 50 Ω resistor that has an 18pF capacitance in parallel. These values correspond to and simulate the signal readout at the oscilloscope and are taken from the data sheet [37].
A screenshot of a typical LTSpice input is shown in figure 6.1. The input for the single pixel in

SN.	SiPM size	C_D / F	$R_{discharge}$ / Ω
1549	1x1,100	$(3.180 \pm 0.005) \cdot 10^{-13}$	0.63
516	3x3,100	$(3.554 \pm 0.006) \cdot 10^{-13}$	0.57
551	3x3,100	$(3.529 \pm 0.005) \cdot 10^{-13}$	0.56
1927	1x1,50	$(5.323 \pm 0.010) \cdot 10^{-14}$	3.76
2889	3x3,50	$(8.329 \pm .0011) \cdot 10^{-14}$	2.40
1067	1x1,25	$(1.314 \pm 0.002) \cdot 10^{-14}$	15.22
1068	1x1,25	$(1.357 \pm 0.003) \cdot 10^{-14}$	14.74
150	3x3,25	$(1.842 \pm 0.002) \cdot 10^{-14}$	10.86
Ketek	3x3,50	$(1.880 \pm 0.008) \cdot 10^{-13}$	1.06

Table 6.1: Resistance values used to discharge the diode capacitance in the simulations, the values for the diode capacitance C_D are taken from the extraction of the electrical parameters (see section 4.3)

LTSpice is shown in figure 6.2.

6.3 Results

Simulations of single pixel breakdowns are carried out. These simulations are then compared to a measured pulse. This measured pulse is the mean of ~ few 100 pulses in order to suppress noise in the shape.

A comparison of the simulated and measured pulse of a Hamamatsu SiPM (1x1,100; SN: 1549) is shown in figure 6.3. Since the signal height depends on the applied overvoltage, which could not be exactly determined for the measurements, the simulated signal was rescaled such that the amount of released charge is equal for measurement and simulation.

The simulated pulse deviates severely from the measured one. The simulated pulse exhibits two components. The first component is a very fast peak component with a duration of $\tau \sim$ ns and deviates from the measured pulse. The second component is much slower with $\tau \sim$ 40 ns and fits to the tail of the measured pulse. The second component shows a time constant for the falling edge in the same order as it is expected using

$$\tau = R_Q \cdot C_D \tag{6.5}$$

as explained in section 5. Please note that the small peak component in the measured signal

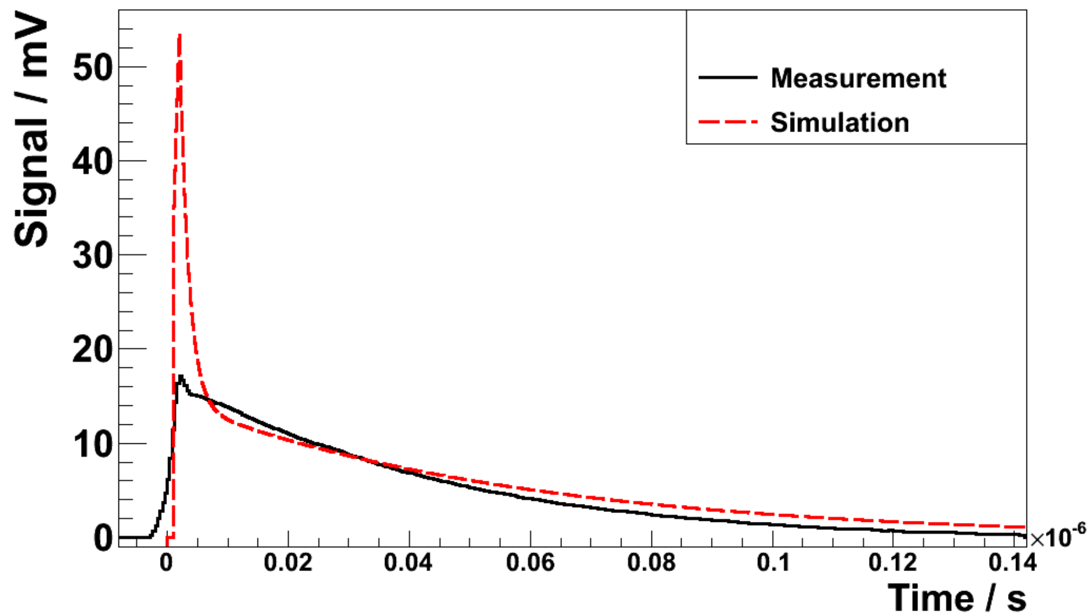

Figure 6.3: Simulation and measurement of a single photon SiPM pulse of a Hamamatsu SiPM (3x3,100), SN: 516 with the original model, simulation signal is rescaled that simulation and measurement release the same amount of charge

is not due to the signal itself. The peakfinder method aligns all pulses at their highest point to calculate the mean of all pulses. It is likely that the highest point of the peak is located shortly after the cell has fired and the noise of the oscilloscope adds a positive signal to the pulse. After this maximum the noise level gets lower and thus reduces the signal. So the reduced noise component after a maximum noise level is visible in the signal trace right after the maximum of the pulse. This, however, has no further effect on the comparison of simulation and measurement.

To understand the deviation between simulation and measurement, the influence of the different components in the circuit (R_Q, C_D, C_Q and C_G) is simulated and analyzed in section 6.5.

6.4 Test of measurement and analysis accuracy

To show that the measurements of the electrical parameters itself are consistent, the impedance of the SiPMs was simulated in the frequency range between 20 Hz and 2 MHz and compared to the impedance measurements. The relative deviation between these data points is shown exemplarily in figure 6.4 for the Hamamatsu SiPM SN: 516 (3x3, 100). The impedance values for the simulation are slightly below the values for the measurement but within the uncertainties. This small underflow can be due to rounding precision during the transfer of the measured properties to the simulation input. All in all, the comparison of the impedance data shows that the measurement and the simulation are consistent with respect to the impedance.

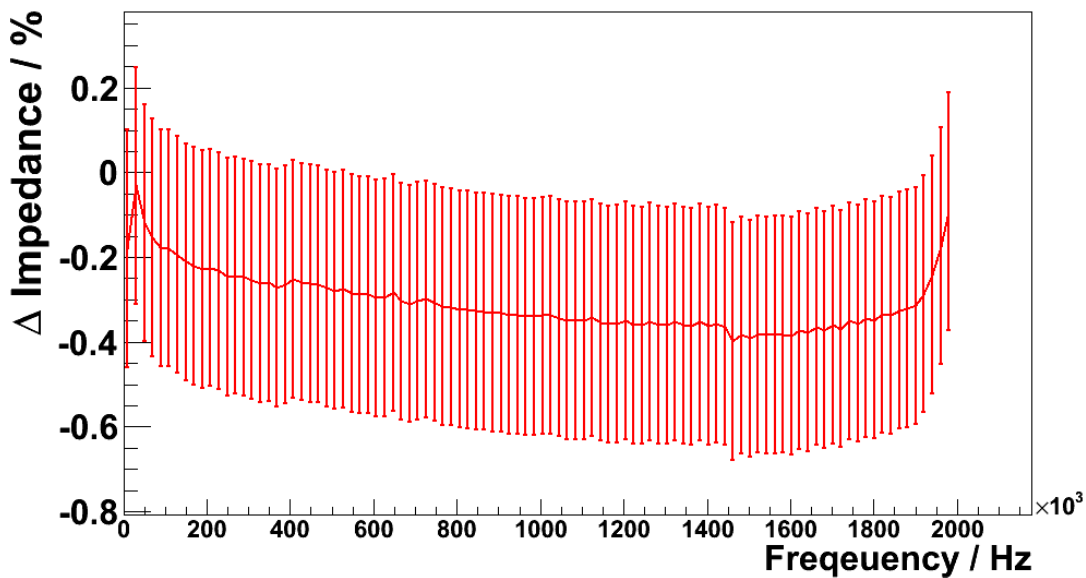

Figure 6.4: Relative deviation of the impedance measurement to the simulation for the Hamamatsu SiPM SN: 516 (3x3, 100)

The impedance values for an SiPM with 100 pixels with defined model parameters (R_Q, C_D, C_Q and C_G) were simulated over 201 steps in the frequency range between 20 Hz - 2 MHz. These are the same conditions as for the impedance measurements (see section 3).
These simulation results were then analyzed in the same way as the measured data to determine if the given uncertainties of the results (see section 4) are reliable. In the data analysis

Parameters	C_D / F	C_Q / F	C_G / F
Simulation*	$3.18 \cdot 10^{-13}$	$71.8 \cdot 10^{-15}$	$6.81 \cdot 10^{-12}$
Analysis*	$(3.15 \pm 0.04) \cdot 10^{-13}$	$(65.0 \pm 11.2) \cdot 10^{-15}$	$(7.17 \pm 0.93) \cdot 10^{-12}$
Simulation 1	$1.59 \cdot 10^{-13}$	$71.8 \cdot 10^{-15}$	$6.81 \cdot 10^{-12}$
Analysis 1	$(1.57 \pm 0.03) \cdot 10^{-13}$	$(80.2 \pm 10.2) \cdot 10^{-15}$	$(6.99 \pm 0.71) \cdot 10^{-12}$
Simulation 2	$4.77 \cdot 10^{-13}$	$71.8 \cdot 10^{-15}$	$6.81 \cdot 10^{-12}$
Analysis 2	$(4.73 \pm 0.05) \cdot 10^{-13}$	$(74.5 \pm 8.19) \cdot 10^{-15}$	$(7.26 \pm 0.68) \cdot 10^{-12}$
Simulation 3	$3.18 \cdot 10^{-13}$	$35.9 \cdot 10^{-15}$	$6.81 \cdot 10^{-12}$
Analysis 3	$(3.14 \pm 0.03) \cdot 10^{-13}$	$(44.5 \pm 13.7) \cdot 10^{-15}$	$(6.77 \pm 0.85) \cdot 10^{-12}$
Simulation 4	$3.18 \cdot 10^{-13}$	$107.6 \cdot 10^{-15}$	$6.81 \cdot 10^{-12}$
Analysis 4	$(3.24 \pm 0.04) \cdot 10^{-13}$	$(111.01 \pm 14.3) \cdot 10^{-15}$	$(7.42 \pm 0.74) \cdot 10^{-12}$
Simulation 5	$3.18 \cdot 10^{-13}$	$71.8 \cdot 10^{-15}$	$3.41 \cdot 10^{-12}$
Analysis 5	$(3.20 \pm 0.04) \cdot 10^{-13}$	$(69.3 \pm 7.8) \cdot 10^{-15}$	$(3.21 \pm 0.49) \cdot 10^{-12}$
Simulation 6	$3.18 \cdot 10^{-13}$	$71.8 \cdot 10^{-15}$	$10.22 \cdot 10^{-12}$
Analysis 6	$(3.17 \pm 0.03) \cdot 10^{-13}$	$(71.1 \pm 8.34) \cdot 10^{-15}$	$(9.96 \pm 1.09) \cdot 10^{-12}$

Table 6.2: Simulation input parameters and measured values for the measurement sensitivity; The simulation marked with * is the simulation with the measured parameters

the quenching resistance was fixed to the model value (118.1 kΩ for all simulations) because the resistance value determination was done before the fit of the data to the impedance formula (see section 4.1). Every parameter was varied by ±50% while the other parameters were kept at their measured value. Thus six simulations (two for every parameter C_D, C_Q and C_G) were conducted plus one simulation with the measured values. All values and the analysis results are shown in table 6.2.

The values from the analysis all agree with the simulated values within approximately one standard deviation. Thus the measurement and analysis method seem to be appropriate for the given model of the SiPM.

6.5 Analysis of model parameters

In this section the impact of the four model parameters (R_Q, C_D, C_Q and C_G) on the signal shape are discussed for an SiPM with 100 pixels. Nevertheless, the conclusions are also valid for SiPMs with higher pixel numbers.

For this analysis every of the four model parameters is varied in seven equidistant steps while

the other parameters are fixed to their default value and a one-pixel pulse is simulated. This family of pulses is then plotted for every model parameter. The default values and variation regimes are shown in table 6.3.

Parameter	Default value	Variation regime
R_Q	118.1 kΩ	98.1 kΩ - 158.1 kΩ
C_D	$3.18 \cdot 10^{-13}$ F	$0.18 \cdot 10^{-13}$ F - $6.18 \cdot 10^{-13}$ F
C_Q	$4.18 \cdot 10^{-15}$ F	$1.18 \cdot 10^{-15}$ F - $7.18 \cdot 10^{-15}$ F
C_G	$6.81 \cdot 10^{-12}$ F	$2.81 \cdot 10^{-12}$ F - $8.81 \cdot 10^{-12}$ F

Table 6.3: Simulation parameters for the analysis of the model parameter's impact on the SiPM signal

6.5.1 Variation of the quenching resistance R_Q

The resulting signal shapes are shown in figure 6.5. The peak height of the fast signal component is almost unaffected by the quenching resistor and decreases only by less than 1 % in the simulated resistance regime. The falling edge of the second component gets steeper for smaller quenching resistances since it is directly correlated to the exponential fall time constant as stated before. The integral over the whole time range is the same for all quenching resistances. Thus the quenching resistor is not responsible for the amount of emitted charge as it is also expected from the model (see section 2).
Since the quenching resistor is often made of polysilicon that shows a strong temperature dependence of the resistivity [39], these variations in the pulse shape should be visible in measured SiPM signals for different temperatures.

6.5.2 Variation of the diode capacitance C_D

The simulation of seven different diode capacitances is shown in figure 6.6.
The slow component of the signal shows a longer tail for higher diode capacitances. This is again due to the diode capacitances' influence on the time constant of the falling edge. It also shows that the integral of the pulses is larger for larger diode capacitances. This is consistent with the expectations since the diode capacitance is discharged in the simulation during the avalanche breakdown which represents the underlying reason for the signal evolution. With a higher diode capacitance the amount of released charge increases $\propto C_\mathrm{D}$.

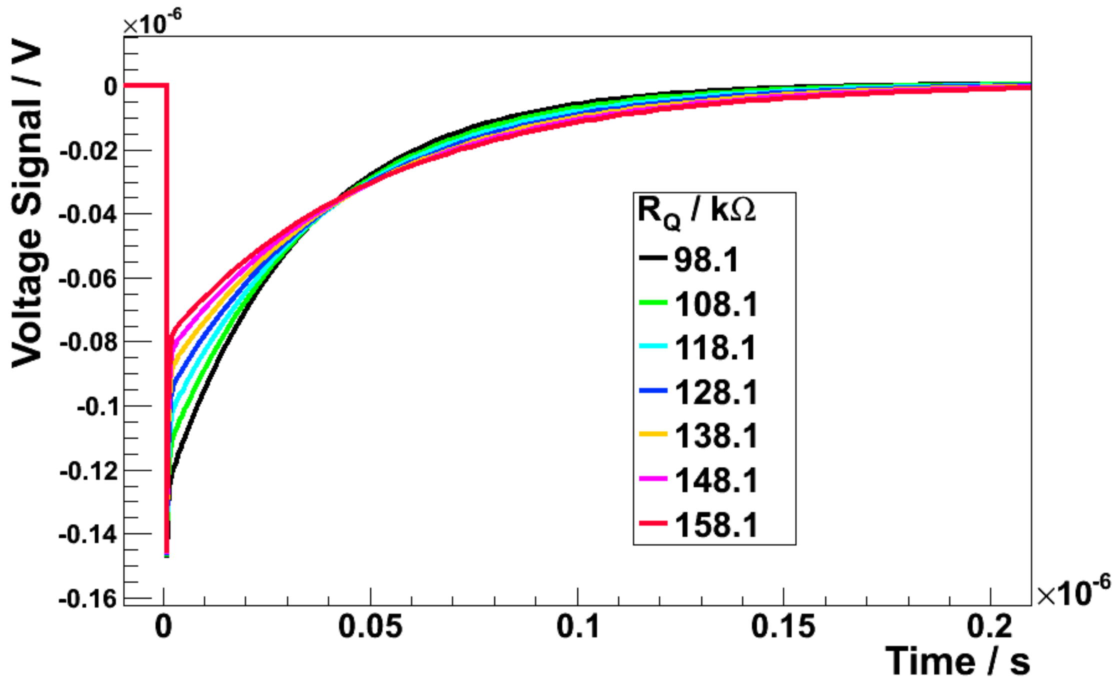

Figure 6.5: Resulting pulse shapes for different quenching resistances for a 100 pixel SiPM (electrical parameters see table 6.3)

The fast component of the signal is again almost uninfluenced. It is apparent that the peak height is slightly higher for smaller diode capacitances. This can be explained by the fact that for small diode capacitances the time constants align more and more. So the second (slow) component adds to the first (fast) one.

6.5.3 Variation of the quenching capacitance C_Q

The resulting pulse shapes for the analysis of the quenching capacitance's input on the pulses are shown in figure 6.7.

The graph shows the first 7 ns of the pulses after the avalanche breakdown since the variation of the quenching capacitance influences only the fast peak component. With decreasing quenching capacitance the fast peak component vanishes. For even lower capacitances the rising edge of the pulse is stretched to $\sim$ 1 ns. So the quenching capacitance seems to play a role relating to the existing fast peak component in the simulation of SiPMs with the mea-

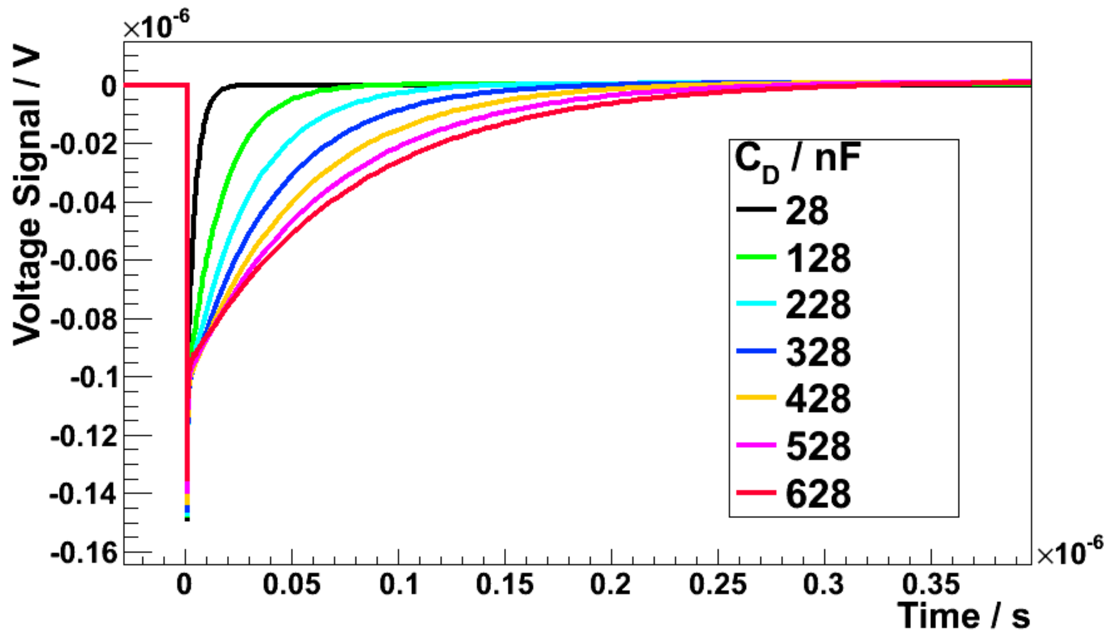

Figure 6.6: Resulting pulse shapes for different diode capacitances for a 100 pixel SiPM (electrical parameters see table 6.3)

sured electrical parameters.

6.5.4 Variation of the grid capacitance C_G

The last of the analyzed parameters is the grid capacitance (C_G). The seven simulated pulses are shown in figure 6.8.

The influence of the grid capacitance seems to have the same structure as the impact of the quenching capacitance. In this case the fast peak component gets smaller for higher grid capacitances. This is vice versa to the influence of the quenching capacitance. The grid capacitance seems to buffer the peak component introduced by the quenching capacitance.

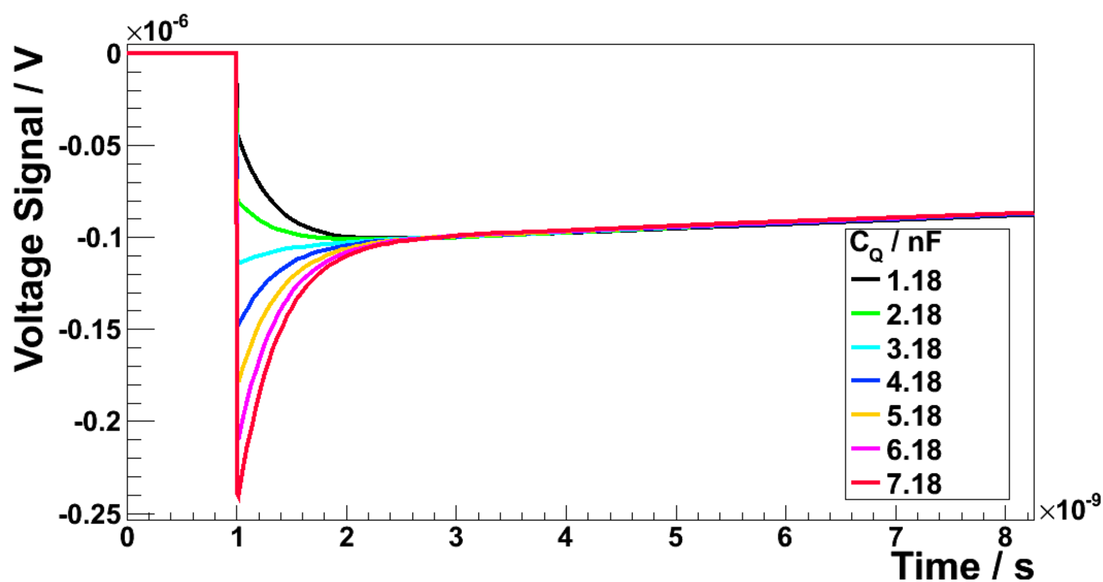

Figure 6.7: Resulting pulse shapes for different quenching capacitances for a 100 pixel SiPM (electrical parameters see table 6.3)

6.6 Correlation between grid and quenching capacitance

To understand the correlation between grid capacitance and quenching capacitance three different cases are considered. The time constants

$$\tau_G = R_G \cdot C_G \tag{6.6}$$

with $R_G = 50\ \Omega$ the resistor that terminates the SiPM to ground and C_G the grid capacitance and

$$\tau_Q = R_Q \cdot C_Q \tag{6.7}$$

are used to define the three cases.
In case of $\tau_G < \tau_Q$ (see figure 6.9) the pulse has the two discussed components. The charge released from the diode capacitance is absorbed by the grid capacitance faster than by the quenching capacitance. This excess of charge that reaches the charged grid capacitance and cannot be absorbed is measured as peak component.
In the case of identical time constants ($\tau_Q = \tau_G$) the effects of peak absorption are exactly

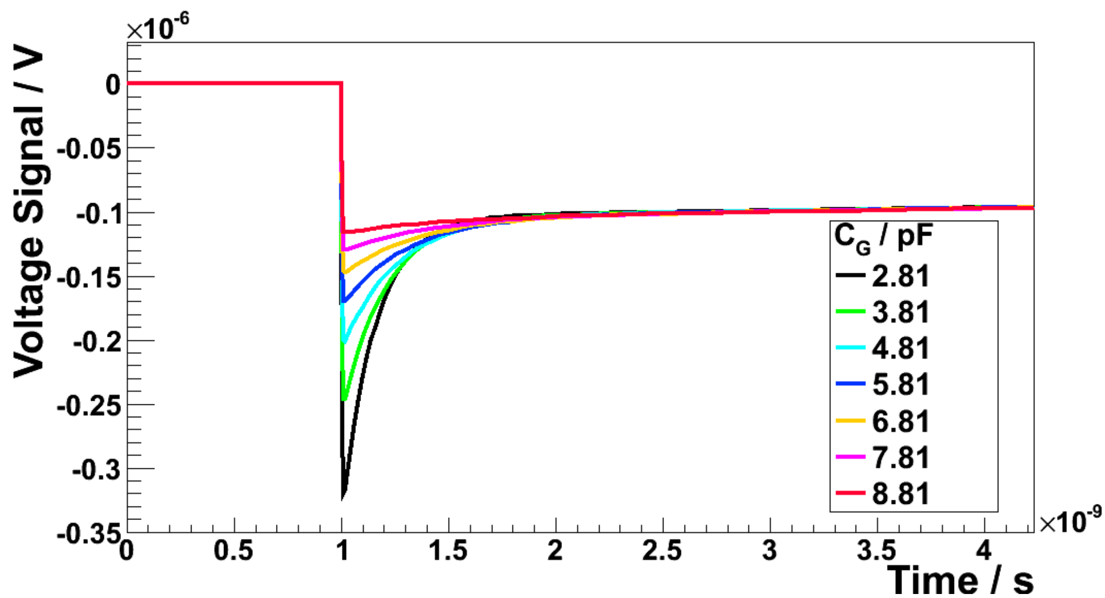

Figure 6.8: Resulting pulse shapes for different grid capacitances for a 100 pixel SiPM (electrical parameters see table 6.3)

compensated. The charge from the diode capacitance can now fill the grid capacitance and the quenching capacitance synchronously. Thus only the peak component generated by the diode capacitance and the quenching resistor remains since the grid capacitance and the quenching capacitance cancel each other.
In the remaining case ($\tau_Q < \tau_G$) the quenching capacitance is charged faster than the grid capacitance. Thus the grid capacitance can buffer the charge for a longer time. This charge is then released afterwards, which smoothens the whole pulse.

6.7 Simulations with adjusted parameters

For the simulation of the given devices the case $\tau_Q > \tau_G$ applies. Since the quenching capacitance is an inherent characteristic of the device, it is most likely that the grid capacitance is responsible for the deviation between measurement and simulation. The impedance measurement was conducted with a calibrated measurement device. The device under test was plugged to the LCR-meter directly. Thus only the connections and wafer effects were taken into account. If the SiPM is operated and read out, readout electronics and power supply are

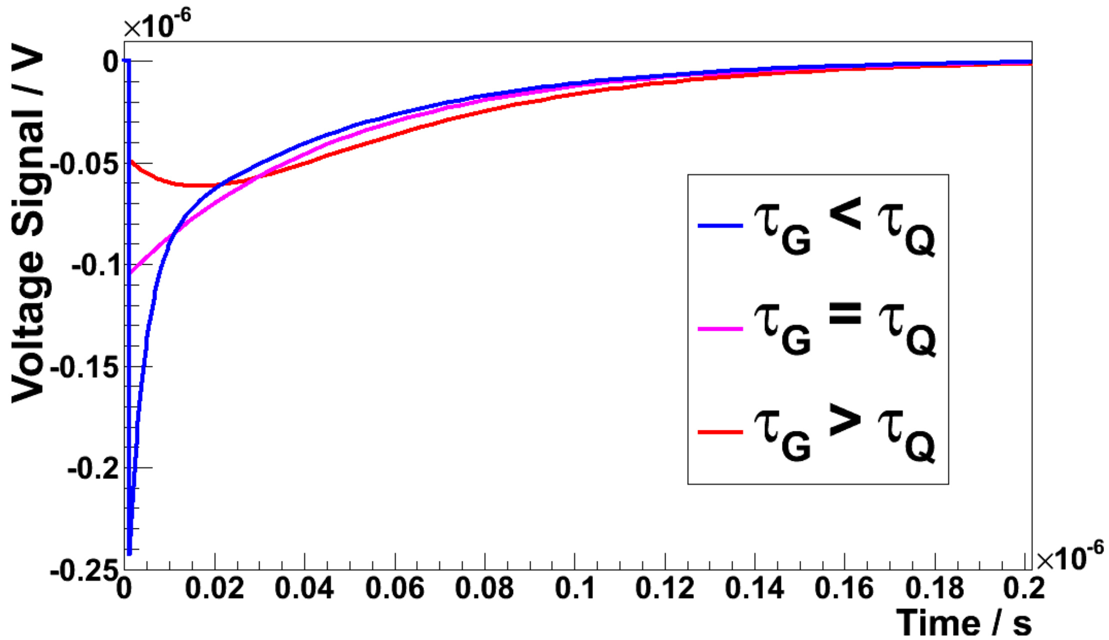

Figure 6.9: Pulse shape for the three different cases $\tau_Q > = < \tau_G$; in case of non-equal values the values differ approximately by a factor 4

attached to the SiPM. The parasitic capacitance of the power supply and of the cabling directly adds up to the grid capacitance because it is also in parallel to the SiPM. A higher grid capacitance leads directly to a larger τ_G. So the height of the peak component is smaller than it would be expected by simulations because the simulations use an ideal voltage source as power supply.

This shows the need of increasing the grid capacitance to simulate a measurement setup close to reality. This effective grid capacitance $C_{G'}$ depends on the readout setup and differs for different setups.

In a next step the parameter τ_G is adjusted in the simulations to obtain a good agreement between measurement and simulation. Therefore, the pulse shape of the Hamamatsu SiPM SN 1067 has been adjusted. The determined value $C_{G'}$ was then used for the simulation of the other SiPMs since the measured pulses were all recorded with the same readout electronics and power supply. Thus one would expect that the value $C_{G'}$ has the same offset for all SiPMs.

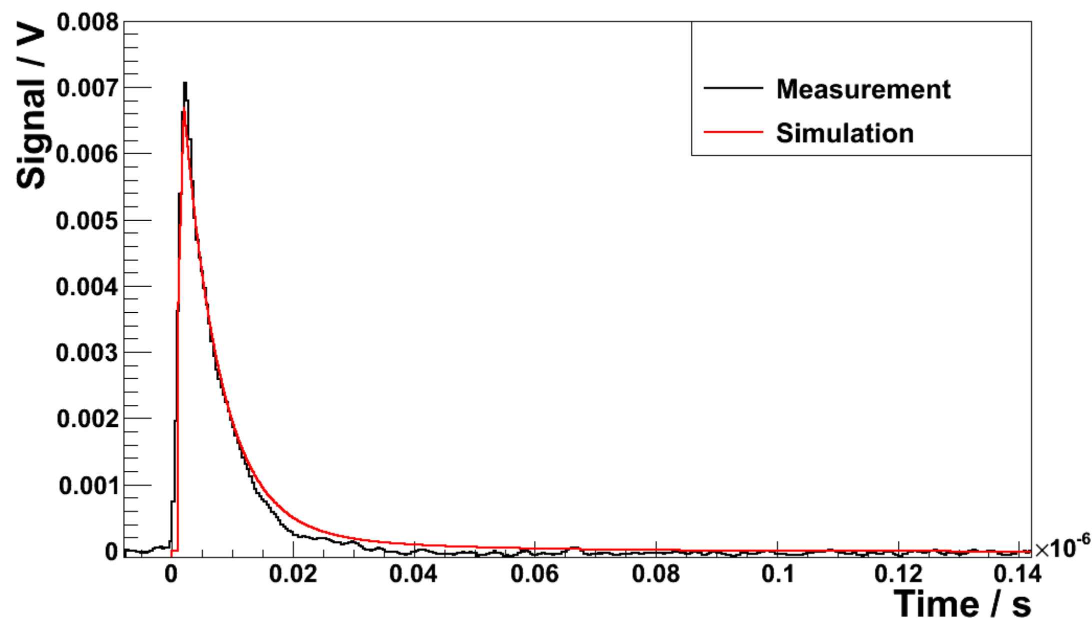

Figure 6.10: Simulated and measured pulse shape for a single pixel breakdown of the Hamamatsu SiPM SN: 1067 (1x1, 25)

The best value was found to be

$$C_{G'} = C_{G_{\text{measured}}} + C_{G_{\text{external}}} \approx C_{G_{\text{external}}} \approx 1.1 \cdot 10^{-10}\ \text{F} \tag{6.8}$$

($C_{G_{\text{measured}}} \ll C_{G_{\text{external}}}$) to simulate the pulses. A measurement of the capacitance at the connection pins of the connection board (cf. section 5.4) with an automatic passive component analyzer [40] provides values in the same order of magnitude as the offset.
A comparison for the resulting simulated single pixel breakdown signal and the measurement is shown for the Hamamatsu SiPMs SN: 1067 (1x1, 25) and SN: 1927 (1x1, 50) in figures 6.10 and 6.11. The simulated pulses for the other SiPMs up to 1600 pixels are shown in the appendix. SiPMs with more than 1600 pixels were not simulated because the simulation time increases with the number of pixels non-linearly, so that the simulation time can reach hours for SiPMs with 3600 pixels and up to a day for SiPMs with 14400 pixels.
Almost all signals show good agreement between measurement and simulation. The Hamamatsu SiPM SN: 1927 (1x1, 50) shows a slightly smaller recovery time in the simulation than

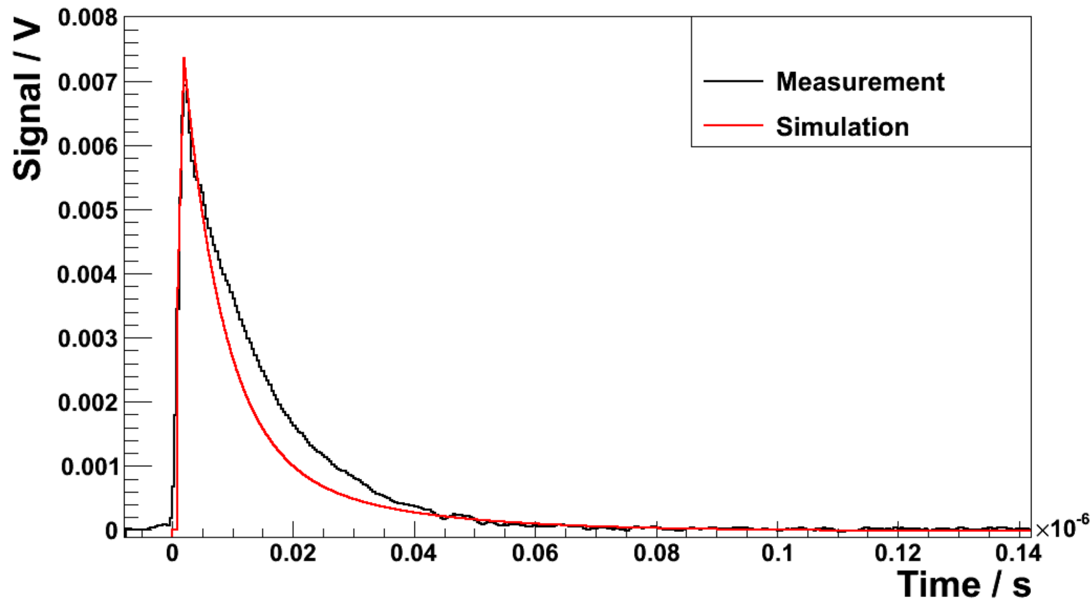

Figure 6.11: Simulated and measured pulse shape for a single pixel breakdown of the Hamamatsu SiPM SN: 1927 (1x1, 50)

in the measurement (see figure 6.11). This difference is already visible in the comparison of measured recovery time and the parameters R_Q and C_D. In this case the average pulse determination showed deficits due to the peak-finder that localized the top of the pulses wrongly for this SiPM.

So the simulation is able to simulate SiPM single pulses with a corresponding pulse shape. The pulse shape is determined by the internal parameters of the SiPM and the used readout electronics and power supply. Therefore, the parameter $C_{G_{\mathrm{external}}}$ has to be determined for a given setup either by measurements or by adjusting an SiPM signal to a measured pulse shape before complex signals can be simulated.

The ability of the simulation model to simulate whole dark noise traces is investigated in the next section.

6.8 Simulation of an event with crosstalk and afterpulsing

Since the simulation simulates every pixel individually, a signal with crosstalk and afterpulsing can also be created.

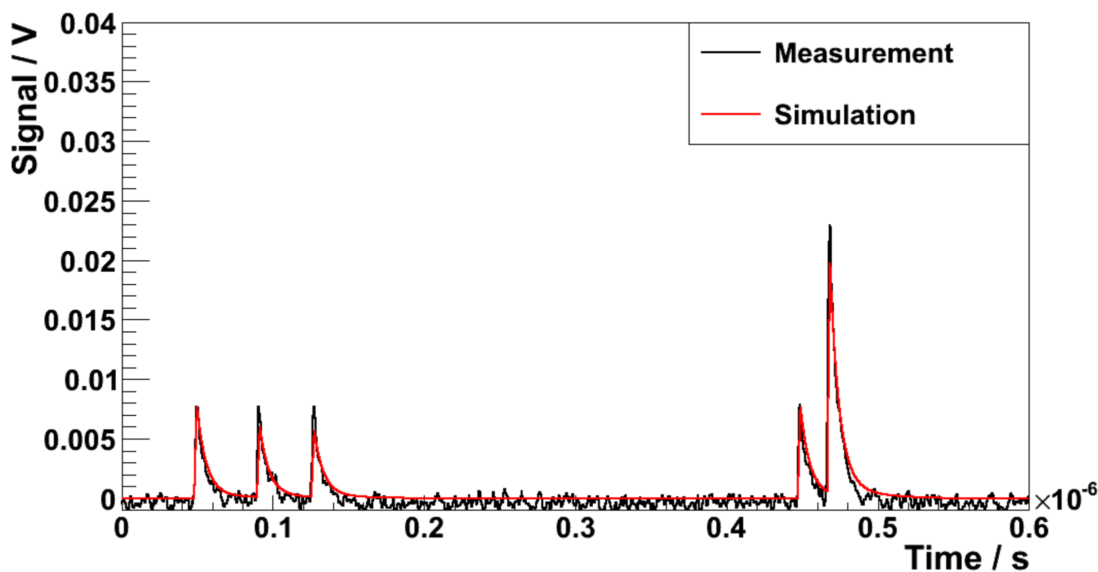

Figure 6.12: Simulated and measured pulse shape for a several single pixel breakdowns and a crosstalk event of the Hamamatsu SiPM SN: 1067 (1x1, 25); only one pixel fires for the first four pulses

To produce the simulated signal the positions (49 ns, 90.5 ns, 126.5 ns, 448 ns, 467.5 ns) and peak heights in terms of p.e. steps of the five measured peaks were determined. For the first four peaks one pixel was fired. For the last peak three pixels were fired due to crosstalk. The pulse might be induced by afterpulsing. Thus the pixel that induced the fourth pulse might contribute to the fifth pulse, too.

Two simulations have been conducted:

1) In the first simulation one single pixel fired during the five peaks. In the last peak two additional pixels fired (see figure 6.12).

2) The second simulation uses different pixels for all peaks. Thus a certain pixel fired only once during the whole simulation time (see figure 6.13).

The peak height in the first simulation of the first three peaks decreases with the number of

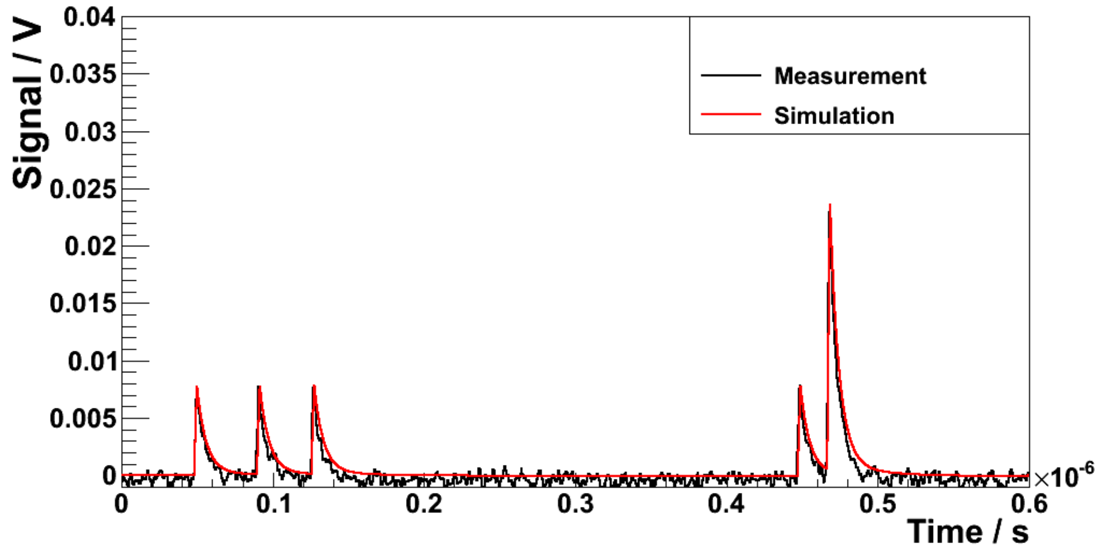

Figure 6.13: Simulated and measured pulse shape for a several single pixel breakdowns and a crosstalk event of the Hamamatsu SiPM SN: 1067 (1x1, 25); every pulse is triggered by a different pixel

pulses. It seems to be due to that the triggered pixel was not fully recharged yet. The fourth peak has the same height as the first one. Here the pixel had enough time after the breakdown to recharge completely. The fifth simulated pulse is smaller than in the measured data. This deficit in the pulse height is also due to the incomplete recharge of the pixel.

The second simulation fits better with the data than the first one. The pulse heights agree. So it seems that the pulses in data are not triggered by one pixel only but by different pixels.

All in all, the simulation is able to simulate noise traces of SiPMs. Moreover, every pixel can be triggered individually so that simulating trigger time stamps from thermal noise rates, crosstalk probabilities and afterpulsing probabilities for every pixel, a dark noise trace can be simulated.

7 Conclusion and Outlook

In this thesis an electrical model for common SiPMs has been successfully adapted using only four intrinsic parameters (R_Q, C_D, C_Q and C_G). This model is able to describe a complex semiconductor device by using only resistors and capacitors.
A measurement method was presented that is capable of measuring these parameters by using an LCR-meter and analyzing the impedance values at the frequency range from 20 Hz - 2 MHz.
Since the diode capacitance C_D is voltage dependent, the measurements have been performed in the voltage range from 0 V up to 40 V. It showed that the quenching resistor and the diode capacitance can be measured with an accuracy of the order of 1% . The quenching capacitance and the grid capacitance values are less accurate, of the order of 10% . So the quenching resistor and the diode capacitance seem to contribute dominantly to the impedance value of the SiPMs in the measured frequency range. The parameters C_Q and C_D might also be a too simple ansatz to describe the parasitic effects in the SiPM correctly over the entire frequency range.
Various Spice simulations of the given model have been performed. These simulations confirmed the sensitivity of the impedance measurements and the used analysis by analyzing simulated data and comparing measured and simulated impedance values.
The simulation of SiPM single pixel events showed that the parameter C_G has to be adjusted for taking into account external electronics. By adjusting this parameter SiPM pulses could be simulated that can reproduce measured pulses reliably. Moreover, SiPM dark noise traces can be simulated with this model that include crosstalk and afterpulsing.

As next steps the measurements could be redone using a measurement device that is able to measure the impedance at a frequency range > 2 MHz to gain more precise information about the quenching capacitance and the grid capacitance. Additionally, measurements with applied reverse bias voltages up to the breakdown voltage of the Hamamatsu SiPMs (~ 70 V) should be performed to investigate the behavior of the diode capacitance at high reverse-bias voltages that had to be extrapolated in this thesis.

Simulations have been performed for SiPMs with a pixel number of up to 1600. With increasing computing capacity simulations of SiPMs with higher pixel numbers will be possible within a reasonable calculation time in the future.
The impedance measurements could be taken at different SiPM temperatures to investigate the impact of the temperature on the quenching resistor and the other parameters.
The simulation model could be extended so that it is able to simulate random noise traces using Monte Carlo trigger time stamps for every single pixel taking into account crosstalk and afterpulsing. Such values have been measured by M. Lauscher and A. Künsken in their respective master theses [17, 41].

A Appendix

A.1 Fully derived impedance formula

$$
\begin{aligned}
|Z(\omega)| = \Bigg(& n^2 R_Q^{-2} \left(R_Q^{-2} + \omega^2 C_Q^2\right)^{-2} \left(\frac{1}{R_Q^2 \left(R_Q^{-2}+\omega^2 C_Q^2\right)^2} + \left(-\frac{\omega C_Q}{R_Q^{-2}+\omega^2 C_Q^2} - \frac{1}{\omega C_D} \right)^2 \right)^{-2} \\
& + \left(-n \left(-\frac{\omega C_Q}{R_Q^{-2}+\omega^2 C_Q^2} - \frac{1}{\omega C_D} \right) \left(\frac{1}{R_Q^2 \left(R_Q^{-2}+\omega^2 C_Q^2\right)^2} + \left(-\frac{\omega C_Q}{R_Q^{-2}+\omega^2 C_Q^2} - \frac{1}{\omega C_D} \right)^2 \right)^{-1} + \omega C_G \right)^2 \Bigg)^{-\frac{1}{2}}
\end{aligned}
\tag{A.1}
$$

This formula shows the impedance of an SiPM assuming the described model (see section 2.4). It is derived from eq. 2.11. A fit of this formula to the impedance measurements yields the electrical parameters of the model (see section 4).

A.2 Additional figures

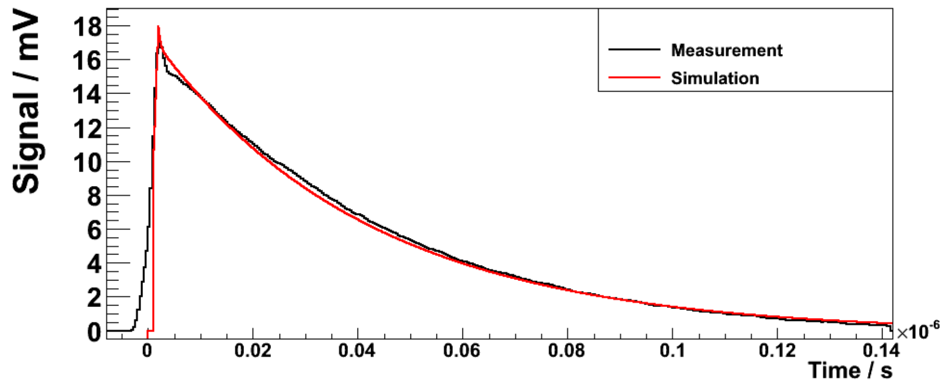

Figure A.1: Simulated and measured pulse shape for a single pixel breakdown of the Hamamatsu SiPM SN: 1549 (1x1, 100)

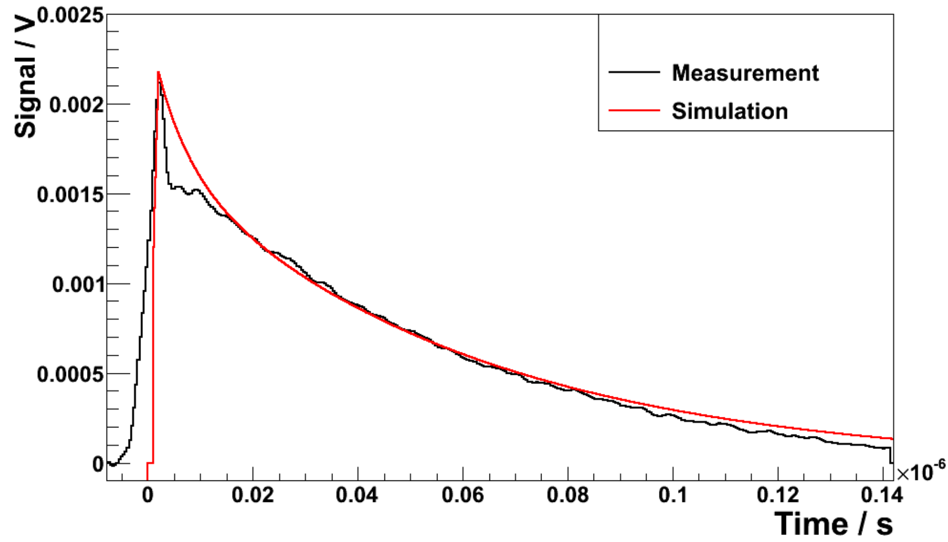

Figure A.2: Simulated and measured pulse shape for a single pixel breakdown of the Hamamatsu SiPM SN: 516 (3x3, 100)

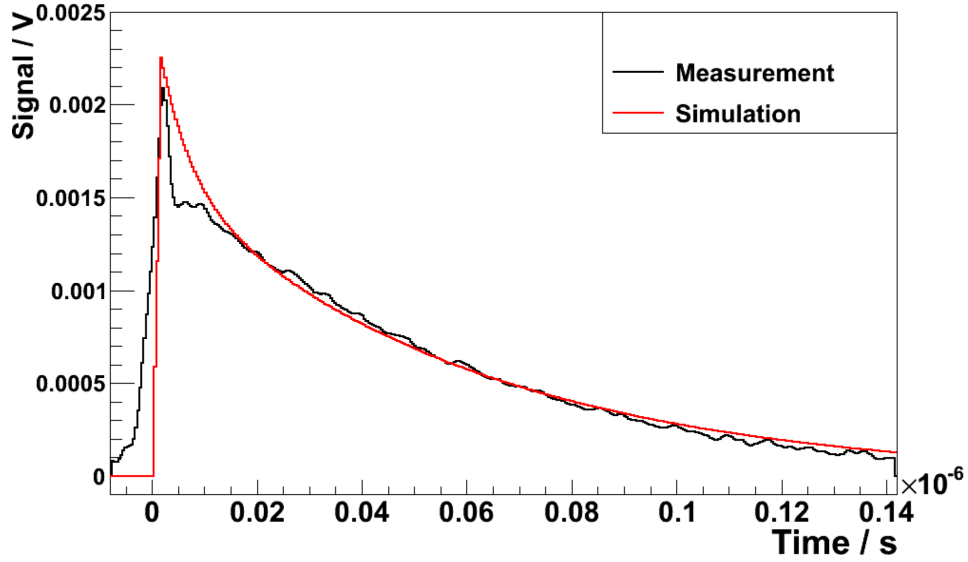

Figure A.3: Simulated and measured pulse shape for a single pixel breakdown of the Hamamatsu SiPM SN: 551 (3x3, 100)

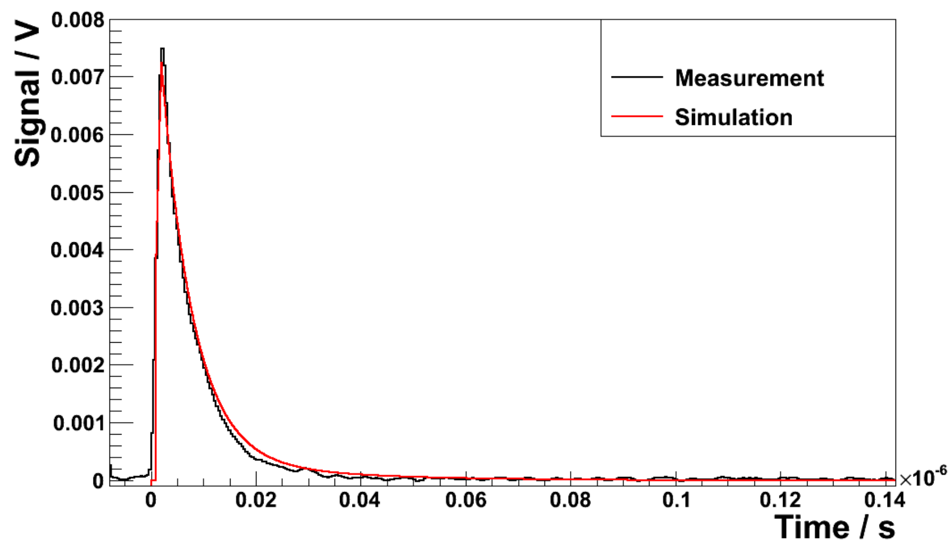

Figure A.4: Simulated and measured pulse shape for a single pixel breakdown of the Hamamatsu SiPM SN: 1068 (1x1, 25)

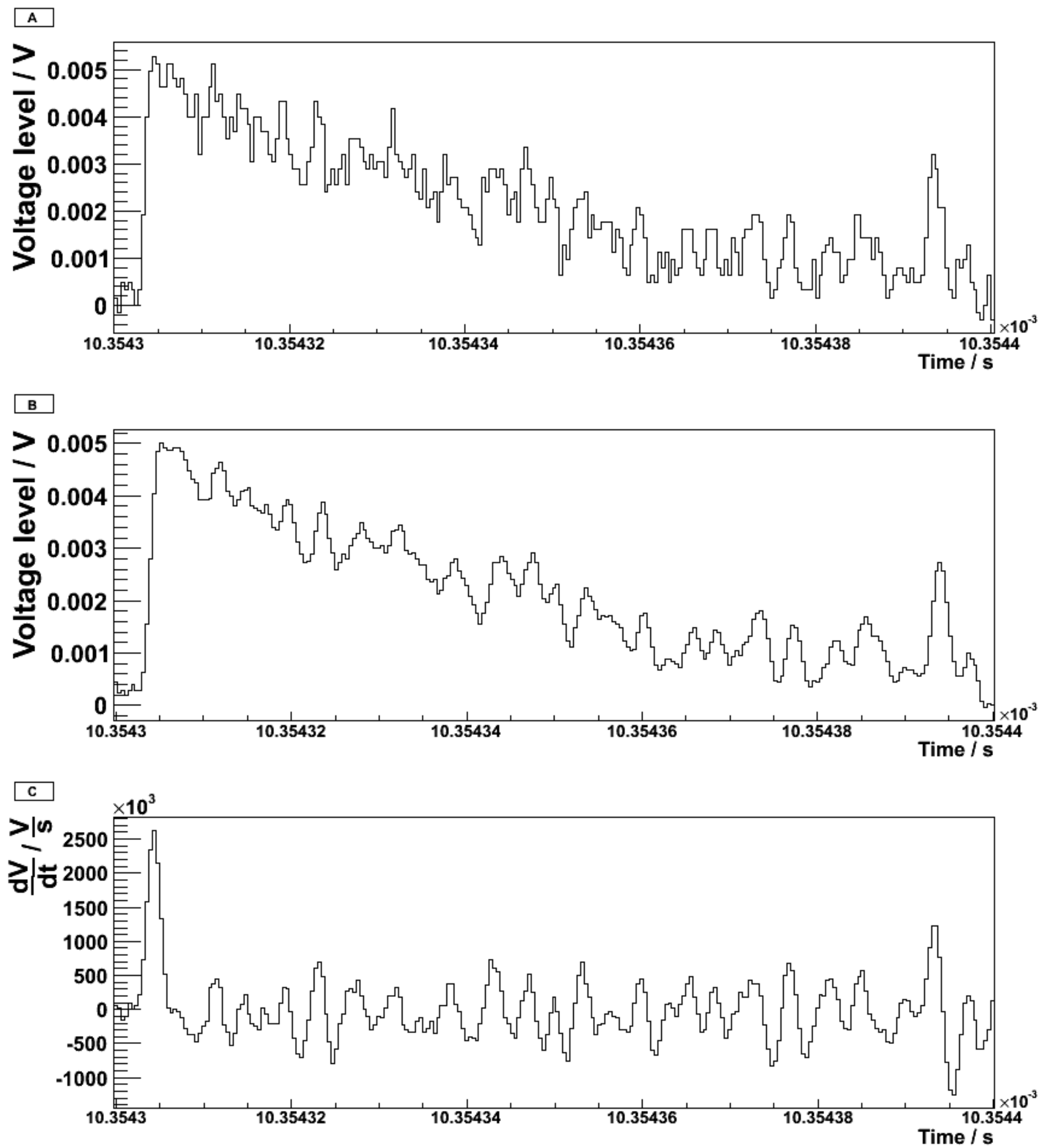

Figure A.5: A) Part of an unprocessed SiPM pulse within a voltage trace; B) Part of a flattened SiPM pulse within a voltage trace; C) Part of the derivative of an SiPM pulse within a voltage trace (the peak at the beginning of the puls is clearly visible; the negative peak at the falling edge of the pulse is too small to be visible because the falling edge is less steep then the rising edge)

Bibliography

[1] Florian Scheuch. Measurements of a detector prototype with direct SiPM read-out and comparison with simulated data. Bachelor's thesis, RWTH Aachen University, 2010.

[2] S. M. Sze, Kwok K. Ng. *Physics of Semiconductor Devices*. John Wiley & Sons, Inc., 3rd edition, 2007.

[3] http://en.wikipedia.org/wiki/Pnjunction, last checked October 29th, 2012. url.

[4] Benjamin Glauss. Optical Test Stand and SiPM characterization studies. Master's thesis, RWTH Aachen University, III. Physikalisches Institut A, 2012.

[5] Jörg Rennefeld. Studien zur Eignung von Silizium Photomultipliern für den Einsatz im erweiterten CMS Detektor SLHC. Diploma thesis, RWTH Aachen University, 2010.

[6] Ivan Rech, Antonino Ingargiola, Roberto Spinelli, Ivan Labanca, Stefano Marangoni, Massimo Ghioni, Sergio Cova. Optical crosstalk in single photon avalanche diode arrays: a new complete model. *Optics Express*, 16(12):8381 – 8394, June 2008.

[7] http://www.home.agilent.com/, last checked Octover 29th, 2012. url.

[8] Agilent Technologies. *Agilent Impedance Measurement Handboook*, 4th edition, 2009.

[9] Patrick Hallen. Determination of the Recovery Time of Silicon Photomultipliers. Bachelor's thesis, RWTH Aachen University, 2011.

[10] Agilent Technologies. *Agilent E4980A Precision LCR Meter*, 8th edition, June 2010.

[11] Artur Lobanov. SiPM Light Mixers for CMS HO Upgrade. Technical report, DESY CMS Group, 2011.

[12] Hamamatsu Photonics K.K. *Photomultiplier Tube R11568*, March 2011.

[13] Maurice Stephan, Thomas Hebbeker, Markus Lauscher, Christine Meurer, Tim Niggemann, Johannes Schumacher, III. Physics Institute A, RWTH Aachen University. *Future*

use of silicon photomultipliers for the fluorescence detection of ultra-high-energy cosmic rays, 2011.

[14] H. Anderhub et al. Results of the Prototype Camera for FACT. *Nuclear Instruments and Methods in Physics Research Section A*, 639(1):55–57, September 2010.

[15] Stefan Seifert, Ruud Vinke, Herman T. van Dam, Herbert Löhner, Peter Dendooven, Freek J. Beekman, Dennis R. Schaart. Ultra Precise Timing with SiPM-Based TOF PET Scintillation Detectors. In *IEEE Nuclear Science Symposium Conference Record*, pages 2329 – 2333, 2009.

[16] Solid State Division Hamamatsu. MPPC Multi-Pixel Photon Counter. Datasheet, September 2010.

[17] Markus Lauscher. Characterisation Studies of Silicon Photomultipliers for the Detection of Fluorescence Light from Extensive Air Showers. Master's thesis, III. Physikalisches Institut A, RWTH Aachen University, January 2012.

[18] Dieter K. Schroder. *Semiconductor Material and Device Characterization*. John Wiley & Sons, Inc., 3rd edition, 2006.

[19] Peter H. Rose, Geoffrey Ryding. Concepts and designs of ion implantation equipment for semiconductor processing. *Review of scientific instruments*, 77(111101):1–12, 2006.

[20] Enrico Fermi translated by A. Zannoni. On the Quantizatoin of the Monoatomic Ideal Gas. *arXiv:cond-mat/9912229v1*, 1926, 1999.

[21] S. Cova, M. Ghioni, A. Lacaita, C. Samori, F. Zappa. Avalanche photodiodes and quenching circuits for single-photon detection. *Applied Optics*, 35(12):1956 – 1976, April 1996.

[22] D. Renkera and E. Lorenz. *Advances in solid state photon detectors*. IOP Publishing, 2009.

[23] Jelena Ninkovic, Ladislav Andricek, Christian Jendrisyk, Gerhard Liemann, Gerhard Lutz, Hans-Günther Moser, Rainer Richter, Florian Schopper. The First measurements on SiPMs with Bulk Integrated Quench Resistors. *Nuclear Instruments and Methods A*, 628(1):407–410, February 2011.

[24] V. Golovin, V. Saveliev. Novel type of avalanche photodetector with Geiger mode operation. *Nuclear Instruments and Methods in Physics Research A*, 518:560 – 564, 2004.

[25] B. Dolgoshein. *Silicon Photomultipliers in Particle Physics: Possibilities and Limitations*, Moscow Engineering and Physics Institute, 2003.

[26] Samuel España, Gustavo Tapias. Performance Evaluation of SiPM Detectors for PET Imaging in the Presence of Magnetic Fields. In *IEEE Nuclear Science Symposium Conference Record*, pages 3591 – 3595, 2008.

[27] Erika Garutti. Silicon photomultipliers for high energy physics detectors. *Nuclear Instruments and Methods A*, 6(C10003):1–14, October 2011.

[28] R. Pagano. Optimized silicon photomultipliers with optical trenches. *Solid-State Device Research Conference (ESSDERC), 2011 Proceedings of the European*, pages 183–186, 2011.

[29] F. Corsi et al. Electrical Characterization of Silicon Photo-Multiplier Detectors for Optimal Front-End Design. In *IEEE Nuclear Science Symposium Conference Record*, pages 1276–1280, 2006.

[30] M.J. Boschini et al. *Electrical Characterization of SiPM as a Function of Test Frequency and Temperature*. Proceedings of the 13th ICATPP Conference on Astroparticle, Particle, Space Physics and Detectors for Physics Applications, Villa Olmo, arXiv:1112.0107 2011.

[31] Wolfgang Demtröder. *Experimentalphysik 2*. Springer-Verlag Berlin Heidelberg New York, 4th edition, 2006.

[32] Elektro-Automatik. Programmable Laboratory Power Supplies EA-PSI 6032-06. Datasheet.

[33] Carsten Heidemann. private communication.

[34] Phillips Scientific. Fast Pulse Preamplifier Model 6954. Datasheet.

[35] Rhode & Schwarz. R&S FSH4/R&S FSH8 Spectrum Analyzer Specifications. Datasheet.

[36] Elektro-Automatik. EA-PS 2000 172W Double Laboratory Power Supplies. Datasheet.

[37] Tektronix. Digital Phosphor Oscilloscopes DPO7000C Series. Datasheet.

[38] L. W. Nagel and D. O. Pederson, Electronics Research Laboratory, College of Engineering, University of California. SPICE. Memorandum No. ERL-M382, 1973.

[39] N. Tomozeiu, S. Antohe, M. Modreanu. Electrical Properties of LPCVD Polysilicon Deposited in the Vincity of Amorphous - Polycristalline Phase. *Journal of Optoelectronics and Advanced Materials*, 2(5):657–663, 2000.

[40] Peak electronic design ltd. Atlas LCR40 passive component analyser. Datasheet.

[41] Andreas Künsken. Simulations of silicon photomultipliers at different operating points and validation by measurements. Master's thesis, RWTH Aachen University, III. Physikalisches Institut A, to be published, 2012.

Acknowledgements

An erster Stelle bedanke ich mich bei Herrn Prof. Dr. Thomas Hebbeker für die Möglichkeit, diese spannende Arbeit an seinem Institut zu verfassen, und die hilfreichen Ratschläge, die diese Masterarbeit bereichert haben.
Ebenso bedanke ich mich bei Herrn Prof. Dr. Christopher Wiebusch, der sich bereit erklärt hat, diese Arbeit als Zweitgutachter zu betreuen.
Viel Unterstützung erhielt ich von Dr. Markus Merschmeyer, der stets mit Rat und Tat zur Seite stand und durch seine Anmerkungen und Verbesserungsvorschläge bezüglich dieser Arbeit maßgeblich zu ihrem Gelingen beigetragen hat.
Einige Messungen habe ich an externen Instituten durchgeführt. Ich danke dafür sehr herzlich dem I. Physikalischen Institut B und Herrn Prof. Dr. Dr. Steffen Leonhardt und Mark Ulbrich vom Philips Lehrstuhl für Medizinische Informationstechnik.
Für sprachliche Korrekturen bedanke ich mich bei meinem Bruder Alexander, der sich bei seinem eigenen vollen Terminplan Zeit genommen hat, diese Arbeit auf Rechtschreibung und Grammatik zu prüfen.
Die Erstellung einer solchen Arbeit bedarf auch immer der Unterstützung und Beratung vieler Kollegen. Diese Unterstützung habe ich bei den „Hallenbewohnern" vorgefunden, die einen stets ermutigt haben, Fragen zu stellen, und angeregte Diskussionspartner waren. Ich fühlte mich vom ersten Tag aufgenommen. Vielen Dank!
Außerdem möchte ich mich auch noch bei meinem langjährigen Mitbewohner Andreas bedanken. Diese Arbeit stellt den Schlusspunkt eines fünfjährigen Studiums dar. Die meiste Zeit habe ich mit Andreas in einer WG gewohnt und gemeinsam mit ihm gelernt und Ablenkung gefunden. Es war eine gute Zeit, auf die ich gerne zurückblicke.
Diese fünf Jahre wurden ebenfalls von meinen Eltern mitgetragen, die mich sowohl finanziell als auch persönlich durch das Studium begleitet haben. Ohne sie wäre es niemals zu dieser Arbeit gekommen.
Selbstverständlich gibt es viele andere Menschen, die in irgendeiner Weise an der Erstellung dieser Arbeit und dem Abschluss meines Studiums beteiligt waren, die ich jedoch nicht einzeln aufzählen kann. Jedem, der sich darauf angesprochen fühlt, gebührt mein Dank.

Erklärung

Ich versichere, diese Arbeit selbstständig verfasst und keine anderen als die angegebenen Hilfsmittel und Quellen benutzt zu haben.
Aachen, 09. November 2012

Florian Scheuch